

# PLSO: A generative framework for decomposing nonstationary timeseries into piecewise stationary oscillatory components

Andrew H. Song<sup>1</sup>, Demba Ba<sup>2</sup>, and Emery N. Brown<sup>3,4,5,6</sup>

<sup>1</sup>Electrical Engineering and Computer Science, Massachusetts Institute of Technology, Cambridge, MA

<sup>2</sup>School of Engineering and Applied Sciences, Harvard University, Cambridge, MA

<sup>3</sup>Department of Brain and Cognitive Sciences, Massachusetts Institute of Technology, Cambridge, MA

<sup>4</sup>Institute of Medical Engineering and Sciences, Massachusetts Institute of Technology, Cambridge, MA

<sup>5</sup>Department of Anesthesia, Critical Care, and Pain Medicine, Massachusetts General Hospital, Boston, MA

<sup>6</sup>Picower Institute of Learning and Memory, Massachusetts Institute of Technology, Cambridge, MA

## Abstract

To capture the slowly time-varying spectral content of real-world time-series, a common paradigm is to partition the data into approximately stationary intervals and perform inference in the time-frequency domain. However, this approach lacks a corresponding nonstationary time-domain generative model for the entire data and thus, time-domain inference occurs in each interval separately. This results in distortion/discontinuity around interval boundaries and, consequently, can lead to erroneous inferences based on any quantities derived from the posterior, such as the phase. To address these shortcomings, we propose the Piecewise Locally Stationary Oscillation (PLSO) generative model for decomposing time-series data with slowly time-varying spectra into several oscillatory, piecewise-stationary processes. PLSO, being a nonstationary time-domain generative model, enables inference on the entire time-series, without boundary effects, and, at the same time, provides a characterization of its time-varying spectral properties. For inference, we propose a novel two-stage algorithm that combines Kalman theory and an accelerated proximal gradient algorithm for the nonconvex objective. We demonstrate these points through experiments on simulated data and real neural data from the rat and the human brain.

## 1 Introduction

With the collection of long time-series now common, in areas such as neuroscience and geophysics, it is important to develop an *inference* framework for data where the stationarity assumption is too restrictive. We restrict our attention to data 1) with spectral properties that change slowly over time and 2) for which decomposition into several oscillatory components is warranted for interpretation, often the case in electroencephalogram (EEG) or electrophysiology recordings. One can use bandpass filtering [Oppenheim et al., 2009] or methods such as the empirical mode decomposition [Huang et al., 1998, Daubechies et al., 2011] for these purposes. However, due to the absence of a generative model, these methods lack a framework for performing inference. Another approach is to perform inference in the time-frequency (TF) domain on the short-time Fourier transform (STFT) of the data, assuming stationarity within small intervals. This has led to a rich literature on inference in the TF domain, such as [Wilson et al., 2008]. A drawback is that most of these methods focus on estimates for the power spectral density (PSD) and lose important phase information. To recover the time-domain estimates, additional algorithms are required [Griffin and Jae Lim, 1984].

This motivates us to explore time-domain generative models that allow time-domain inference and decomposition into oscillatory components. We can find examples based on the stationarity assumption in the signal processing/Gaussian process (GP) communities. A superposition of stochastic harmonic oscillators, where each oscillator corresponds to a frequency band, is used in the processing of speech [Cemgil and Godsill, 2005] and neuroscience data [Matsuda and Komaki, 2017, Beck et al., 2018]. In the GP literature [Rasmussen and Williams, 2005], the spectral mixture (SM) kernel [Wilson and Adams, 2013, Wilkinson et al., 2019] models the data as samples from a GP, whose kernel consists of the superposition of localized and frequency-modulated kernels.

These time-domain models can be applied to nonstationary data by partitioning them into stationary intervals. Compared to STFT-based methods, these models retain phase information. This allows time-domain inference within each interval. However, we are faced with a different kind of challenge. As the inference is localized within each interval, the time-domain estimates in different intervals are independent conditioned on the data and do not reflect the dependence across intervals. This also causes discontinuity/distortion of the time-domain estimates near the interval boundaries, and consequently any quantities derived from these estimates.

To address these shortcomings, we propose a generative framework for data with slow time-varying spectra, termed the Piecewise Locally Stationary Oscillation (PLSO) framework. The main contributions are:

**Generative model for piecewise stationary, oscillatory components** PLSO models time-series as the superposition of piecewise stationary, oscillatory components. This allows time-domain inference on each component and estimation of the time-varying spectra.

**Continuity across stationary intervals** The state-space model that underlies PLSO strikes a balance between ensuring time-domain continuity across piecewise stationary intervals and stationarity within each interval. Moreover, by imposing stochastic continuity on the interval-level, PLSO learns underlying smooth time-varying spectra accurately.

**Inference procedure** We propose a two-stage inference procedure for the time-varying spectra and the time-series. By leveraging the Markovian dynamics, the algorithm combines Kalman filter theory [Kalman, 1960] and inexact accelerated proximal gradient approach [Li and Lin, 2015].

In Section 2 we introduce necessary background, followed by the PLSO framework in Section 3. In Section 4, we discuss inference for PLSO. In Section 5, we discuss how PLSO relates to other frameworks. In Section 6, we present experimental results and conclude in Section 7.

## 2 Background

### 2.1 Notation

We use  $j \in \{1, \dots, J\}$  and  $k \in \{1, \dots, K\}$  to denote frequency and discrete-time sample index, respectively. We use  $\omega \in [-\pi, \pi]$  for normalized frequency. The  $j^{\text{th}}$  latent process centered at  $\omega = \omega_j$  is denoted as  $\mathbf{z}_j \in \mathbb{C}^K$ , with  $\mathbf{z}_{j,k} \in \mathbb{C}$  denoting the  $k^{\text{th}}$  sample of  $\mathbf{z}_j$  and  $\mathbf{z}_{j,k}^{\Re}$ ,  $\mathbf{z}_{j,k}^{\Im}$  its real and imaginary parts. We also represent  $\mathbf{z}_{j,k}$  as a  $\mathbb{R}^2$  vector,  $\tilde{\mathbf{z}}_{j,k} = [\mathbf{z}_{j,k}^{\Re}, \mathbf{z}_{j,k}^{\Im}]^T$ . The elements of  $\mathbf{z}_j$  are denoted as  $\mathbf{z}_{j,k:k'} = [\mathbf{z}_{j,k}, \dots, \mathbf{z}_{j,k'}]^T$ . The state covariance matrix for  $\mathbf{z}_{j,k}$  is defined as  $\mathbf{P}_k^j = \mathbb{E}[\tilde{\mathbf{z}}_{j,k}(\tilde{\mathbf{z}}_{j,k})^T]$ . To express an enumeration of variables, we use  $\{\cdot\}$  and drop first/last index for simplicity, e.g.  $\{\mathbf{z}_j\}_j$  instead of  $\{\mathbf{z}_j\}_{j=1}^J$ .

We focus on the discrete-time framework and use  $\mathbf{y}_k$  and  $\mathbf{z}_{j,k}$  for the discrete-time counterpart of the continuous observation and latent process,  $y(t)$  and  $z_j(t)$ . With the sampling frequency  $f_s = 1/\Delta$ , we have  $\mathbf{y}_k = y(k\Delta)$ ,  $\mathbf{z}_{j,k} = z_j(k\Delta)$ , and  $T = K\Delta$ .

### 2.2 Piecewise local stationarity

The concept of *piecewise local stationarity* (PLS) for nonstationary time-series with slowly time-varying spectra [Adak, 1998] plays an important role in PLSO. A stationary process has a constant mean and a covariance function which depends only on the difference between two time points.

For our purposes, it suffices to understand the following on PLS: 1) It includes local stationary [Priestley, 1965, Dahlhaus, 1997] and amplitude-modulated stationary processes. 2) A PLS process can be approximated as a piecewise stationary (PS) process (Theorem 1 of [Adak, 1998])

$$z(t) = \sum_{m=1}^M \mathbf{1}(u_m \leq t < u_{m+1}) \cdot z^{(m)}(t), \quad (1)$$

where  $z^{(m)}(t)$  is a continuous stationary process and the boundaries are  $0 = u_1 < \dots < u_{M+1} = T$ . Note that Eq. 1 does not guarantee continuity across different PS intervals,

$$\lim_{t \rightarrow u_m^-} z(t) = \lim_{t \rightarrow u_m^-} z^{(m-1)}(t) \neq \lim_{t \rightarrow u_m^+} z^{(m)}(t) = \lim_{t \rightarrow u_m^+} z(t).$$

## 3 The PLSO model and its mathematical properties

Building on the Theorem 1 of [Adak, 1998], PLSO models nonstationary data as PS processes. It is a superposition of  $J$  different PS processes  $\{\mathbf{z}_j\}_j$ , with  $\mathbf{z}_j$  corresponding to an oscillatory process centered at frequency  $\omega_j$ . PLSO also guarantees stochastic continuity across PS intervals. We show that piecewise stationarity and continuity across PS intervals are two competing objectives and that PLSO strikes a balance between them, as discussed in Section 3.2.

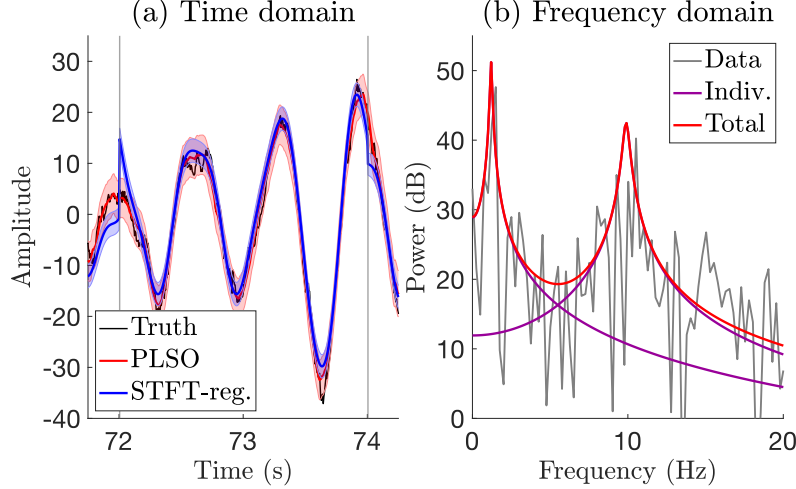


Figure 1: A simulated example. (a) Time domain. Data (black) around boundaries (gray) and inferred oscillatory components using PLSO (red) and regularized STFT (blue). (b) Frequency domain. Spectrum of the data (gray), PLSO components for  $J = 2$  (purple) and their sum (red).

Fig. 1 shows an example of the PLSO framework applied to simulated data. In the time domain, the oscillation inferred using the regularized STFT (blue) [Kim et al., 2018], which imposes stochastic continuity on the STFT coefficients, suffers from discontinuity/distortion near window boundaries, whereas that inferred by PLSO (red) does not. In the frequency domain, each PLSO component corresponds to a localized spectrum  $S_j(\omega)$ , the sum of which is the PSD  $\gamma(\omega)$ , and is fit to the data STFT  $I(\omega)$ . We start by introducing the PLSO model for a single window.

### 3.1 PLSO for stationary data

As a building block for PLSO, we use the discrete stochastic harmonic oscillator for a stationary time series [Qi et al., 2002, Cemgil and Godsill, 2005, Matsuda and Komaki, 2017]. The data  $\mathbf{y}$  are assumed to be a superposition of  $J$

zero-mean components

$$\begin{aligned}\tilde{\mathbf{z}}_{j,k} &= \rho_j \mathbf{R}(\omega_j) \tilde{\mathbf{z}}_{j,k-1} + \varepsilon_{j,k} \\ \mathbf{y}_k &= \sum_{j=1}^J \mathbf{z}_{j,k}^{\mathfrak{R}} + \nu_k,\end{aligned}\tag{2}$$

where  $\mathbf{R}(\omega_j) = \begin{pmatrix} \cos(\omega_j) & -\sin(\omega_j) \\ \sin(\omega_j) & \cos(\omega_j) \end{pmatrix}$ ,  $\varepsilon_{j,k} \sim \mathcal{N}(0, \alpha_j \mathbf{I}_{2 \times 2})$ , and  $\nu_k \sim \mathcal{N}(0, \sigma_{\nu}^2)$ , correspond to a rotation matrix, the state noise, and the observation noise, respectively. We reparameterize  $\rho_j$  and  $\alpha_j$ , using lengthscale  $l_j$  and power  $\sigma_j^2$ , such that  $\rho_j = \exp(-\Delta/l_j)$  and  $\alpha_j = \sigma_j^2(1 - \rho_j^2)$ . This establishes the equivalent continuous model in the form of stochastic differential equation [Solin and Särkkä, 2014], further explored in the next section and the **Appendix A**.

In the time domain, assuming  $\mathbf{P}_1^j = \sigma_j^2 \mathbf{I}_{2 \times 2} \forall j$ , the autocovariance is given as  $\mathbb{E}[\mathbf{z}_{j,k}^{\mathfrak{R}} \mathbf{z}_{j,k+n'}^{\mathfrak{R}}] = \sum_{j=1}^J \sigma_j^2 \exp(-n' \Delta/l_j)$ . In the frequency domain, the spectra for the  $j^{\text{th}}$  component,  $S_j(\omega)$ , and the PSD for  $\mathbf{y}$ ,  $\gamma(\omega)$ , are given by

$$\begin{aligned}S_j(\omega) &= \varphi_j(\omega) + \varphi_j(-\omega), \quad \gamma(\omega) = \sigma_{\nu}^2 + \sum_{j=1}^J S_j(\omega) \\ \varphi_j(\omega) &= \frac{\sigma_j^2 (1 - \exp(-2\Delta/l_j))}{1 + \exp(-2\Delta/l_j) - 2 \exp(-\Delta/l_j) \cos(\omega - \omega_j)}.\end{aligned}$$

The lengthscale  $l_j$  controls the bandwidth of the  $j^{\text{th}}$  process, with *large*  $l_j$  corresponding to *narrower* bandwidth. The variance  $\sigma_j^2$  controls the overall power of  $\mathbf{z}_j$ , along with  $l_j$ . Note that the magnitude of  $\varphi_j(\omega)$ , and consequently  $S_j(\omega)$ , is maximized at  $\omega = \pm \omega_j$ .

### 3.2 PLSO for nonstationary data

For the nonstationary case, we first partition  $\mathbf{y}$  into  $M$  non-overlapping intervals, indexed by  $m \in \{1, \dots, M\}$ , of length  $N$ , indexed by  $n \in \{1, \dots, N\}$ , such that  $K = MN$ . We then apply the stationary PLSO to each interval, with additional Markovian dynamics imposed on  $\sigma_{j,m}^2$ ,

$$\begin{aligned}\log(\sigma_{j,m}^2) &= \log(\sigma_{j,m-1}^2) + (1/\sqrt{\lambda})\eta_{j,m} \\ \tilde{\mathbf{z}}_{j,mN+n} &= \exp(-\Delta/l_j) \mathbf{R}(\omega_j) \tilde{\mathbf{z}}_{j,mN+(n-1)} \\ &\quad + \varepsilon_{j,mN+n} \\ \mathbf{y}_{mN+n} &= \sum_{j=1}^J \mathbf{z}_{j,mN+n}^{\mathfrak{R}} + \nu_{mN+n},\end{aligned}\tag{3}$$

where  $\varepsilon_{j,mN+n} \sim \mathcal{N}(0, \sigma_{j,m}^2(1 - \exp(-2\Delta/l_j)) \mathbf{I}_{2 \times 2})$ , with  $\nu_{mN+n}, \eta_{j,m} \sim \mathcal{N}(0, 1)$ . We define  $\mathbf{P}_{m,n}^j$  as the covariance of  $\tilde{\mathbf{z}}_{j,mN+n}$ , with  $\mathbf{P}_{1,1}^j = \sigma_j^2 \mathbf{I}_{2 \times 2}, \forall j$ . The graphical model for the PLSO generative model is shown in Fig. 2.

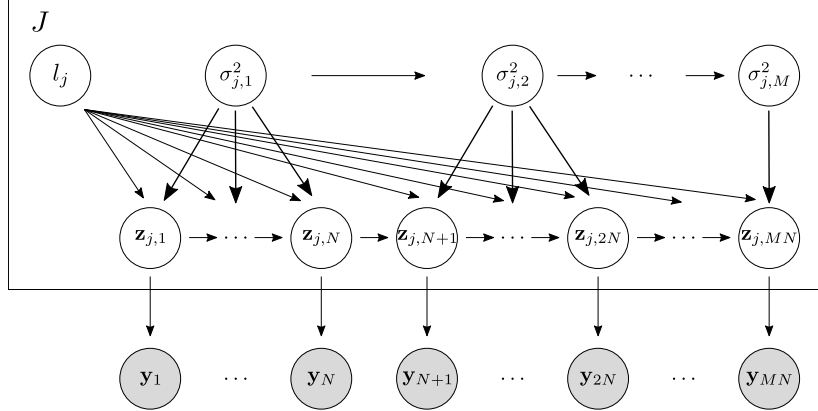


Figure 2: The graphical model for PLSO.

The variance  $\sigma_{j,m}^2$  changes across different intervals and results in time-varying spectra  $S_j^{(m)}(\omega)$  and PSD  $\gamma^{(m)}(\omega)$ . We assume constant lengthscale  $l_j$  to ensure that differences in  $S_j^{(m)}(\omega)$  are caused only by differences in  $\{\sigma_{j,m}^2\}_{j,m}$ .

Given the generative model in Eq. 3, our goal is to perform inference on the posterior distribution

$$\begin{aligned}p(\{\mathbf{z}_j\}_j, \{\sigma_{j,m}^2\}_{j,m} \mid \mathbf{y}, \theta) &= p(\{\sigma_{j,m}^2\}_{j,m} \mid \mathbf{y}, \theta) \cdot p(\{\mathbf{z}_j\}_j \mid \{\sigma_{j,m}^2\}_{j,m}, \mathbf{y}, \theta),\end{aligned}\tag{4}$$

window-level posterior      sample-level posterior

with the parameters  $\theta = \{\lambda, \sigma_{\nu}^2, \{l_j\}_j, \{\omega_j\}_j\}$ . We can learn the parameters, as discussed in Section 4, or fix the parameters to specific values informed by domain knowledge, such as the center frequency or bandwidth of the processes. We first analyze several properties of the PLSO model.

#### 3.2.1 Stochastic continuity

We discuss two types of stochastic continuity, 1) at the window boundaries and 2) on  $\{\sigma_{j,m}^2\}$ .

**Continuity across the window boundaries** In the PLSO model, the state-space model (Eq. 3) provides stochastic continuity across different PS intervals. The following proposition rigorously explains stochastic continuity for PLSO.

**Proposition 1.** For a given  $m$ , as  $\Delta \rightarrow 0$ , the samples on either side of the interval boundary, which are  $\tilde{\mathbf{z}}_{j,(m+1)N}$  and  $\tilde{\mathbf{z}}_{j,(m+1)N+1}$ , become equivalent,

$$\lim_{\Delta \rightarrow 0} \tilde{\mathbf{z}}_{j,(m+1)N} = \lim_{\Delta \rightarrow 0} \tilde{\mathbf{z}}_{j,(m+1)N+1}.$$

*Proof.* We use the connection between PLSO, which is a discrete-time model, and its continuous-time counterpart. Details are in the **Appendix B**.  $\square$

This matches our intuition that as  $\Delta \rightarrow 0$ , the adjacent samples from the same process should get closer to each other until they become equivalent in the limit. If  $\lim_{\Delta \rightarrow 0} \tilde{\mathbf{z}}_{j,(m+1)N} \neq \lim_{\Delta \rightarrow 0} \tilde{\mathbf{z}}_{j,(m+1)N+1}$ , the process is discontinuous, which is the case for PS approaches without continuity. This holds even when the parameters of different intervals are linked through continuity constraints [Rosen et al., 2009, Kim et al., 2018, Song et al., 2018, Soulard et al., 2019] or a hierarchical model [Gramacy and Lee, 2008].

We can interpret the continuity in the context of posterior for  $\mathbf{z}_j$ . For PS approaches without continuity, we have

$$p(\{\mathbf{z}_j\}_j | \mathbf{y}) \propto \prod_{m=1}^M p(\{\mathbf{z}_{j,(m-1)N+1:mN}\}_j | \mathbf{y}_{(m-1)N+1:mN}), \quad (5)$$

where  $\{\sigma_{j,m}^2\}_{j,m}$  and  $\theta$  are omitted for notational ease. This results from  $p(\{\mathbf{z}_j\}_j) = \prod_{m=1}^M p(\{\mathbf{z}_{j,(m-1)N+1:mN}\}_j)$ , due absence of continuity across the windows. Consequently, the time-domain inference results are conditionally independent across the windows. In PLSO, the time-domain estimates depend on the entire observation  $\mathbf{y}$ , not just on a subset.

**Continuity on  $\sigma_{j,m}^2$**  For a given  $j$ , we impose stochastic continuity on  $\log \sigma_{j,m}^2$ . Effectively, this pools together estimates of  $\{\sigma_{j,m}^2\}_m$  to 1) prevent overfitting to the noisy spectra and 2) estimate smooth dynamics of  $\{\sigma_{j,m}^2\}_m$ . The use of  $\log \sigma_{j,m}^2$  ensures that  $\sigma_{j,m}^2$  is non-negative.

The choice of  $\lambda$  dictates the smoothness of  $\{\sigma_{j,m}^2\}_m$ , with the two extremes corresponding to the familiar dynamics. If  $\lambda \rightarrow 0$ , we treat each window independently. If  $\lambda \rightarrow \infty$ , we treat the data as stationary, as the constraint forces  $\sigma_{j,m}^2 = \sigma_j^2, \forall m$ . Practically, the smooth regularization prevents artifacts in the spectral analysis, such as those due to sudden motion or missing data, as demonstrated in Section 6.

### 3.2.2 Piecewise stationarity

For the  $m^{\text{th}}$  window to be piecewise stationary, the initial state covariance matrix  $\mathbf{P}_{m,1}^j$  should be the *steady-state* covariance matrix for the window, denoted as  $\mathbf{P}_{m,\infty}^j$ . This ensures the covariance is stationary within each window.

The challenge is transitioning from  $\mathbf{P}_{m,\infty}^j$  to  $\mathbf{P}_{m+1,\infty}^j$ . If these were equal, a stationary model would apply to the data. Specifically, to ensure  $\mathbf{P}_{m+1,1}^j = \mathbf{P}_{m+1,\infty}^j$ , given that  $\mathbf{P}_{m,N}^j = \mathbf{P}_{m,\infty}^j$ , the *variance* of the process noise between the two samples,  $\varepsilon_{j,(m+1)N+1}$ , has to equal  $\mathbf{P}_{m+1,\infty}^j - \exp(-2\Delta/l_j) \mathbf{P}_{m,\infty}^j$ .

However, this is infeasible. If  $\mathbf{P}_{m+1,\infty}^j < \mathbf{P}_{m,\infty}^j$ , the variance is negative. Even if it were positive, the limit as  $\Delta \rightarrow 0$  does not equal zero, i.e.,  $\mathbf{P}_{m+1,\infty}^j - \mathbf{P}_{m,\infty}^j$ . Consequently, the Proposition 1 no longer holds and the trajectory is discontinuous. In summary, there exists a *trade-off* between maintaining piecewise stationarity and continuity across intervals.

PLSO maintains continuity across the intervals while ensuring that the state covariance quickly transitions to the steady-state covariance. We quantify the speed of transition in the following proposition.

**Proposition 2.** Assume  $l_j \ll N\Delta$ , such that  $\mathbf{P}_{m,N}^j = \mathbf{P}_{m,\infty}^j$ . In Eq. 3, the difference between  $\mathbf{P}_{m,\infty}^j = \sigma_{j,m}^2 \mathbf{I}_{2 \times 2}$  and  $\mathbf{P}_{m+1,\infty}^j = \sigma_{j,m+1}^2 \mathbf{I}_{2 \times 2}$  decays exponentially fast as a function of  $n$ ,

$$\mathbf{P}_{m+1,n}^j = \mathbf{P}_{m+1,\infty}^j + \exp(-2n\Delta/l_j) (\mathbf{P}_{m,\infty}^j - \mathbf{P}_{m+1,\infty}^j).$$

*Proof.* In **Appendix C**, we prove this result by induction.  $\square$

This implies that, except for the transition portion at the beginning of each window, we can assume stationarity. In practice, we additionally impose an upper bound on  $l_j$  during estimation and also use a reasonably-large  $N$ . Empirically, we observe that the transition period has little impact.

## 4 Inference

The posterior distribution factorizes into two terms as in Eq. 4: The *window-level* posterior  $p(\{\sigma_{j,m}^2\}_{j,m} | \mathbf{y}, \theta)$  and the *sample-level* posterior  $p(\{\mathbf{z}_j\}_j | \{\sigma_{j,m}^2\}_{j,m}, \mathbf{y}, \theta)$ . Accordingly, we break the inference into two stages.

**Stage 1** We minimize the *window-level* negative log-posterior, with respect to  $\theta$  and  $\{\sigma_{j,m}^2\}_{j,m}$ .

**Stage 2** Given the estimates  $\{\hat{\sigma}_{j,m}^2\}_{j,m}$  and  $\hat{\theta}$  from Stage 1, we perform inference on the *sample-level* posterior. This includes the mean trajectory  $\tilde{\mathbf{z}}_j = \mathbb{E}[\mathbf{z}_j | \{\hat{\sigma}_{j,m}^2\}_{j,m}, \mathbf{y}, \hat{\theta}]$  and its credible intervals, or any statistical quantity of interest.

We examine each stage in the following sections.

### 4.1 Optimization of $p(\{\sigma_{j,m}^2\}_{j,m} | \mathbf{y}, \theta)$

We factorize the posterior,  $p(\{\sigma_{j,m}^2\}_{j,m} | \mathbf{y}, \theta) \propto p(\mathbf{y} | \{\sigma_{j,m}^2\}_{j,m}, \theta) \cdot p(\{\sigma_{j,m}^2\}_{j,m} | \theta)$ . Due to the intractability of exact inference, we instead minimize the negative log-posterior,  $-\log p(\{\sigma_{j,m}^2\}_{j,m} | \mathbf{y}, \theta)$ . For the log-likelihood  $f(\{\sigma_{j,m}^2\}_{j,m}; \theta) = \log p(\mathbf{y} | \{\sigma_{j,m}^2\}_{j,m}, \theta)$ , we use the *Whittle likelihood* [Whittle, 1953] defined in the frequency domain and which is nonconvex,

$$f(\{\sigma_{j,m}^2\}_{j,m}; \theta) = -\frac{1}{2} \sum_{m=1}^M \sum_{n=1}^N \left\{ \log \gamma^{(m)}(\omega_n) + \frac{I^{(m)}(\omega_n)}{\gamma^{(m)}(\omega_n)} \right\}, \quad (6)$$

with discrete frequency  $\omega_n = 2\pi n/N$ , and periodogram for the  $m^{\text{th}}$  window  $I^{(m)}(\omega_n)$ ,

$$I^{(m)}(\omega_n) = \left| \sum_{n'=1}^N \exp\left(-\frac{2\pi i(n'-1)(n-1)}{N}\right) \mathbf{y}_{mN+n'} \right|^2.$$

The Whittle likelihood enables frequency-domain parameter estimation as a computationally more efficient alternative to the time domain estimation [Turner and Sahani, 2014]. The concave log-prior  $g(\{\sigma_{j,m}^2\}_{j,m}; \theta) = \log p(\{\sigma_{j,m}^2\}_{j,m} | \theta)$ , which arises from the continuity on  $\{\sigma_{j,m}^2\}_{j,m}$ , is given as

$$g(\{\sigma_{j,m}^2\}_{j,m}; \theta) = -\frac{\lambda}{2} \sum_{j=1}^J \sum_{m=1}^M (\log \sigma_{j,m}^2 - \log \sigma_{j,m-1}^2)^2. \quad (7)$$

This yields the following nonconvex problem

$$\begin{aligned} & \min_{\{\sigma_{j,m}^2\}_{j,m}, \theta} -\log p(\{\sigma_{j,m}^2\}_{j,m} | \mathbf{y}, \theta) \\ &= \min_{\{\sigma_{j,m}^2\}_{j,m}, \theta} -f(\{\sigma_{j,m}^2\}_{j,m}; \theta) - g(\{\sigma_{j,m}^2\}_{j,m}; \theta). \end{aligned} \quad (8)$$

We optimize Eq. 8 by block coordinate descent [Wright, 2015] on  $\{\sigma_{j,m}^2\}_{j,m}$  and  $\{\sigma_\nu^2, \{l_j\}_j, \{\omega_j\}_j\}$ . For  $\sigma_\nu^2$ ,  $\{l_j\}_j$ , and  $\{\omega_j\}_j$ , we minimize  $-f(\{\sigma_{j,m}^2\}_{j,m}; \theta)$ , since  $g(\{\sigma_{j,m}^2\}_{j,m}; \theta)$  does not affect them. We perform conjugate gradient descent on  $\{l_j\}_j$  and  $\{\omega_j\}_j$ . We discuss initialization and how to estimate  $\sigma_\nu^2$  in the **Appendix D**.

#### 4.1.1 Optimization of $\{\sigma_{j,m}^2\}_{j,m}$

We introduce an algorithm to compute a local optimal solution of  $\{\sigma_{j,m}^2\}_{j,m}$  for the nonconvex optimization problem in Eq. 8, by leveraging the regularized temporal structure of  $\{\sigma_{j,m}^2\}_{j,m}$ . It extends the inexact accelerated proximal gradient (APG) method [Li and Lin, 2015], by solving the proximal step with a Kalman filter/smooth [Kalman, 1960]. To see this, we note that computing the proximal operator for  $g(\{\sigma_{j,m}^2\}_{j,m}; \theta)$  is equivalent to MAP estimation for  $J$  independent 1-dimensional linear Gaussian state-space models

$$\begin{aligned} & \{\log \sigma_{j,m}^{(l+1),2}\}_{j,m} = \text{prox}_{-\alpha^{(l)} g}(\mathbf{v}^{(l)}) \\ &= \arg \min_{\{\sigma_{j,m}^2\}_{j,m}} \underbrace{\frac{\sum_{j,m}^{J,M} (\mathbf{v}_{j,m}^{(l)} - \log \sigma_{j,m}^2)^2}{2\alpha^{(l)}}}_{\sum_{j=1}^J q_j} - g(\{\sigma_{j,m}^2\}_{j,m}) \end{aligned} \quad (9)$$

where  $\alpha^{(l)} > 0$  is a step-size for the  $l^{\text{th}}$  iteration and

$$\begin{aligned} q_j &= \sum_{m=1}^M \frac{(\mathbf{v}_{j,m}^{(l)} - \log \sigma_{j,m}^2)^2}{2\alpha^{(l)}} + \frac{\lambda}{2} (\log \sigma_{j,m}^2 - \log \sigma_{j,m-1}^2)^2 \\ \mathbf{v}_{j,m}^{(l)} &= \log \sigma_{j,m}^{(l),2} + \alpha^{(l)} \frac{\partial f(\{\sigma_{j,m}^2\}_{j,m})}{\partial \log \sigma_{j,m}^2} \Big|_{\{\sigma_{j,m}^2\}_{j,m} = \{\sigma_{j,m}^{(l),2}\}_{j,m}}. \end{aligned}$$

The  $j^{\text{th}}$  optimization problem,  $\min_{\{\sigma_{j,m}^2\}_{j,m}} q_j$ , is equivalent to estimating the mean of the posterior for  $\{\log \sigma_{j,m}^2\}_m$  in a linear Gaussian state-space model with observations  $\{\mathbf{v}_{j,m}^{(l)}\}_m$ , observation noise variance  $\alpha^{(l)}$ , and state variance  $1/\lambda$ . Therefore, the solution can efficiently be computed with  $J$  parallel, 1-dimensional, Kalman filters/smoothers, with the computational complexity of  $O(JM)$ .

Note that Eq. 9 holds for all non-negative  $\lambda$ . If  $\lambda = 0$ , the proximal operator is an identity operator, as  $\log \sigma_{j,m}^{(l+1),2} = \mathbf{v}_{j,m}^{(l)}$ . This is a gradient descent with a step-size rule. If  $\lambda \rightarrow \infty$ , we have  $\log \sigma_{j,m}^2 = \log \sigma_{j,m-1}^2, \forall m$ , which leads to  $\log \sigma_{j,m}^{(l+1),2} = (1/M) \sum_{m=1}^M \mathbf{v}_{j,m}^{(l)}$ . The algorithm is guaranteed to converge when  $\alpha^{(l)} < 1/C$ , where  $C$  is the Lipschitz constant for  $f(\{\sigma_{j,m}^2\}_{j,m}; \theta)$ . In practice, we select  $\alpha^{(l)}$  according to the step-size rule [Barzilai and Borwein, 1988]. In **Appendix E & F**, we present the full algorithm for optimizing  $\{\sigma_{j,m}^2\}_{j,m}$  and a derivation for  $C$ .

#### 4.2 Inference for $p(\{\mathbf{z}_j\}_j | \{\sigma_{j,m}^2\}_{j,m}, \mathbf{y}, \theta)$

We perform inference on the sample-level posterior distribution  $p(\{\mathbf{z}_j\}_j | \{\hat{\sigma}_{j,m}^2\}_{j,m}, \mathbf{y}, \hat{\theta})$ . Since this is a Gaussian distribution, the mean trajectories  $\{\hat{\mathbf{z}}_j\}_j$  and the credible intervals can be computed analytically. Moreover, Eq. 3 is a linear Gaussian state-space model, we can use Kalman filter/smooth for efficient computation, with computational complexity  $O(J^2K)$ . In **Appendix G**, we discuss these steps.

##### 4.2.1 Monte Carlo Inference

We can also obtain posterior samples and perform Monte Carlo (MC) inference on any posterior-derived quantity. To generate the MC trajectory samples, we use the forward-filter backward-sampling (FFBS) algorithm [Carter and Kohn, 1994]. Assuming  $S$  number of MC samples, the computational complexity for FFBS is  $O(SJ^2K)$ , since for each sample, the algorithm uses Kalman filter/smooth for sampling. This is different from generating samples with the interval-specific posterior in Eq. 5. In the latter case, the FFBS algorithm is run  $M$  separate times, the samples of which have to be pieced together to form an entire trajectory. With PLSO, the trajectory sample is conditioned on the entire observation and is continuous across the intervals.

One quantity of interest is the *phase*. We obtain the phase as  $\phi_{j,k} = \tan^{-1}(\mathbf{z}_{j,k}^{\mathfrak{I}} / \mathbf{z}_{j,k}^{\mathfrak{R}})$ . Since  $\tan^{-1}(\cdot)$  is a non-linear operation, we compute the mean and credible interval with MC samples through the FFBS algorithm. Given the posterior-sampled trajectories  $\{\mathbf{z}_j^{(s)}\}_{j,s}$ , where  $s \in \{1, \dots, S\}$  denotes MC sample index, we estimate the phase as  $\hat{\phi}_{j,k} = (1/S) \sum_{s=1}^S \tan^{-1}(\mathbf{z}_{j,k}^{\mathfrak{I},(s)} / \mathbf{z}_{j,k}^{\mathfrak{R},(s)})$ , and use empirical quantiles for the associated credible interval.

### 4.3 Choice of $J$ and $\lambda$

We choose  $J$  that minimizes the Akaike Information Criterion (AIC) [Akaike, 1981], defined as

$$\text{AIC}(J) = -(2/M) \cdot \log p(\mathbf{y} \mid \{\hat{\sigma}_{j,m}^2\}_{j,m}, \hat{\theta}) + 2 \cdot 3 \cdot J, \quad (10)$$

where  $\hat{\theta}$  and  $\{\hat{\sigma}_{j,m}^2\}_{j,m}$  are the maximum-likelihood fit, and  $3 \cdot J$  is the number of parameters ( $\{l_j\}_j, \{\omega_j\}_j, \{\sigma_{j,m}^2\}_j$ ). The regularization parameter  $\lambda$  is determined through a two-fold cross-validation, where each fold is generated by aggregating even/odd sample indices [Ba et al., 2014].

## 5 Related works

We now examine how PSLO relates to other nonstationary frameworks.

**STFT/Regularized STFT** In STFT, the harmonic basis is used, whereas quasi-periodic components are used for PLSO, which allows capturing of broader spectral content. Recent works regularize STFT coefficients with stochastic continuity across the windows, to infer smooth spectral dynamics [Ba et al., 2014, Kim et al., 2018]. However, this regularization leads to discontinuities at window boundaries.

**Piecewise stationary GP** GP regression and kernel parameter estimation is performed within each window [Gramacy and Lee, 2008, Solin et al., 2018]. Consequently, the recovered trajectories are discontinuous. Also, the inversion of covariance matrix leads to an expensive inference. For example, the time-complexity of mean trajectory estimation is  $O(MN^3) = O(N^2K)$ , whereas the time-complexity for PLSO is  $O(J^2K)$ . Considering that the typical sampling frequency for electrophysiology data is  $\sim 10^3$  (Hz) and windows are several seconds, which leads to  $N \sim 10^3$ , PLSO is computationally more efficient. In the **Appendix H**, we confirm this through an experiment.

**Time-varying Autoregressive model (TVAR)** The TVAR model [Kitagawa and Gersch, 1985] is given as

$$\mathbf{y}_k = \sum_{p=1}^P a_{p,k} \mathbf{y}_{k-p} + \varepsilon_k,$$

with the time-varying coefficients  $\{a_{p,k}\}_p$ . Consequently, it does not suffer from discontinuity issues. TVAR can also be *approximately* decomposed into oscillatory components via eigen-decomposition of the transition matrix [West et al., 1999]. However, since the eigen-decomposition changes at every sample, this leads to an ambiguous interpretation of the oscillations present in the data, as we discuss further in Section 6.

## 6 Experiments

We apply PLSO to three settings: 1) A simulated dataset 2) local-field potential (LFP) data from the rat hippocampus, and 3) EEG data from a subject under anesthesia.

We use PLSO with  $\lambda = 0$ ,  $\lambda \rightarrow \infty$ , and  $\lambda$  determined by cross-validation,  $\lambda_{\text{CV}}$ . We use PS interval lengths chosen by domain experts. As baselines, we use 1) regularized STFT (STFT-reg.) and 2) Piecewise stationary GP (GP-PS). For GP-PS, we use the same  $\{\hat{\sigma}_{j,m}^2\}_{j,m}$  and  $\hat{\theta}$  as PLSO with  $\lambda = 0$ , so that the estimated PSD of GP-PS and PLSO are identical. This lets us explain differences in time-domain estimates by the fact that PSLO operates in the time-domain.

### 6.1 Simulated dataset

We simulate from the following model for  $1 \leq k \leq K$

$$\mathbf{y}_k = 10 \left( \frac{K-k}{K} \right) \mathbf{z}_{1,k}^{\mathfrak{R}} + 10 \cos^4(2\pi\omega_0 k) \mathbf{z}_{2,k}^{\mathfrak{R}} + \nu_k,$$

where  $\mathbf{z}_{1,k}$  and  $\mathbf{z}_{2,k}$  are as in Eq. 2, with  $(\omega_0, \omega_1, \omega_2) = (0.04, 1, 10)$  Hz,  $f_s = 200$  Hz,  $T = 100$  seconds,  $l_1 = l_2 = 1$ , and  $\nu_k \sim \mathcal{N}(0, 25)$ . This stationary process comprises two amplitude-modulated oscillations, namely one modulated by a slow-frequency sinusoid and the other a linearly-increasing signal [Ba et al., 2014]. Additional details are provided in the **Appendix I**.

**Results** We simulate 20 realizations and train on each realization, assuming 2-second PS intervals. For PLSO, we use  $J = 2$ . The averaged results are shown in Table 1. We define  $\text{jump}(\mathbf{z}_j) = \frac{1}{M-1} \sum_{m=1}^{M-1} |\hat{\mathbf{z}}_{j,mN+1} - \hat{\mathbf{z}}_{j,mN}|$  to be the level of discontinuity at the interval boundaries. If  $\text{jump}(\mathbf{z}_j)$  greatly exceeds  $\text{jump}(\mathbf{z}_j^{\text{True}})$ , this implies the existence of large discontinuities at the boundaries.

For GP-PS and STFT-reg.,  $\text{jump}(\mathbf{z}_j)$  exceeds  $\text{jump}(\mathbf{z}_j^{\text{True}})$ , indicating discontinuities at the boundaries. An example is in Fig. 1. PLSO produces a similar jump metric as the ground truth metric, indicating the absence of discontinuities. We attribute the lower value to Kalman smoothing. For the TF domain, we use Itakura-Saito (IS) divergence [Itakura and Saito, 1970] as a distance measure between the ground truth spectra and the PLSO estimates. That the highest divergence is given by  $\lambda \rightarrow \infty$  indicates the inaccuracy of the stationarity assumption.

Table 1: Simulation results. For  $\text{jump}(\mathbf{z}_j)$  and MSE, left/right metrics correspond to  $\mathbf{z}_1/\mathbf{z}_2$ , respectively.

	$\text{jump}(\mathbf{z}_j)$	MSE	IS div.
Truth	0.95/12.11	0/0	0
$\lambda = 0$	0.26/10.15	2.90/3.92	4.08
$\lambda \rightarrow \infty$	0.22/10.32	3.26/4.53	13.78
$\lambda = \lambda_{\text{CV}}$	0.25/10.21	<b>2.88/3.91</b>	<b>3.93</b>
STFT-reg.	49.59/81.00	6.89/10.68	N/A
GP-PS	16.99/23.28	3.00/4.04	4.08

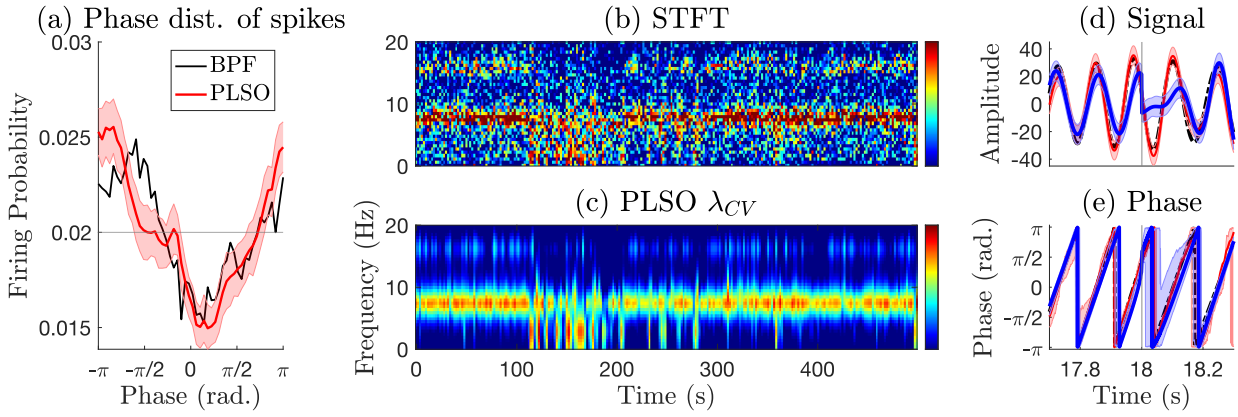


Figure 3: Result of analyses of hippocampal data. (a) Theta phase distribution of population neuron spikes, computed with bandpass-filtered LFP (black), PLSO estimate of  $\hat{\mathbf{z}}_2$  with credible intervals estimated from 200 posterior samples (red). Horizontal gray line indicates the uniform distribution. (b-c) Spectrogram (in dB) for 500 seconds (b) STFT (c) PLSO with  $\lambda_{CV}$ . Learned frequencies are  $(\hat{\omega}_1, \hat{\omega}_2, \hat{\omega}_3) = (2.99, 7.62, 15.92)$  Hz, with  $\hat{\omega}_4 \sim \hat{\omega}_5 > 25$  Hz. (d-e) Time-domain results. (d) Reconstructed signal (e) phase for  $\hat{\mathbf{z}}_2$  and interval boundary (vertical gray), with bandpass-filtered data (dotted black), STFT-reg. (blue), and PLSO (red). Shaded area represents 95% credible interval from  $S = 200$  sample trajectories.

## 6.2 LFP data from the rat hippocampus

We use LFP data collected from the rat hippocampus during open field tasks [Mizuseki et al., 2009], with  $T = 1,600$  seconds and  $f_s = 1,250$  Hz<sup>1</sup>. The theta neural oscillation band ( $5 \sim 10$  Hz) is believed to play a role in coordinating the firing of neurons in the entorhinal-hippocampal system and is important for understanding the local circuit computation.

We fit PLSO with  $J = 5$ , which minimizes AIC as shown in Table 2, with 2-second PS interval. The estimated  $\hat{\omega}_2$  is 7.62 Hz in the theta band. To obtain the phase for non-PLSO methods, we perform the Hilbert transform on the theta-band reconstructed signal. With no ground truth, we bandpass-filter (BPF) the data in the theta band for reference.

Table 2: AIC as a function of  $J$  for Hippocampus data

J	1	2	3	4	5	6
AIC	2882	2593	2566	2522	<b>2503</b>	2505

**Spike-phase coupling** Fig. 3(a) shows the theta phase distribution of population neuron spikes in the hippocampus. The PLSO-estimated distribution (red) confirms the original results analyzed with bandpass-filtered signal (black) [Mizuseki et al., 2009]—the hippocampal spikes show a strong preference for a specific phase,  $\pi$  for this dataset, of the theta band. Since PLSO provides posterior sample-trajectories for the entire time-series, we can compute as many realizations of the phase distribution as the number of MC samples. The resulting credible interval excludes the uniform distribution (horizontal gray), suggesting the statistical significance of strong phase preference.

**Denoised spectrogram** Fig. 3(b-c) shows the estimated spectrogram. We observe that PLSO denoises the spectrogram, while retaining sustained power at  $\hat{\omega}_2 = 7.62$  Hz and weaker bursts at  $(\hat{\omega}_1, \hat{\omega}_3) = (2.99, 15.92)$  Hz.

**Time domain discontinuity** Fig. 3(d-e) show a segment of the estimated signal and phase near a boundary for  $\hat{\omega}_2$ . While the estimates from STFT-reg. (blue) and PLSO (red) follow the BPF result closely, the STFT-reg. estimates exhibit discontinuity/distortion near the boundary. In Fig. 3(e), the phase jump at the boundary is 38.4 degrees. For further analysis, we computed  $\text{jump}(\phi_2)$  in degrees/sample for the phase. Considering that the theta band roughly progresses  $2.16 (= 7.5(\text{Hz}) \times 360/1250(\text{Hz}))$  degrees per sample, we observe that BPF (2.23), as expected, and PLSO ( $\lambda_{CV} : 2.40, \lambda \rightarrow \infty : 2.66$ ) are not affected by the boundary effect. This is not the case for STFT-reg. (26.83) and GP-PS (25.91).

**Comparison with TVAR** Fig. 4(a-b) shows a segment of TVAR inference results<sup>2</sup>. Specifically, Fig. 4(a) and (b) shows a time-varying center frequency  $\hat{\omega}_1$  and the corresponding reconstruction, for the lowest frequency component. Note that the eigenvalues, which correspond to  $\{\omega_j\}_j$ , and the eigenvectors, which are used for oscillatory decomposition, are derived from the *estimated* TVAR transition matrix. Consequently, we cannot explicitly control  $\{\omega_j\}_j$ , as shown in Fig. 4(a), the bandwidth of each component, as well as the number of components  $J$ . This is further complicated by the fact that the transition matrix changes every sample. Fig. 4(b) shows that this ambiguity results in the lowest-frequency component of TVAR explaining *both* the slow ( $0.1 \sim 2$  Hz) and theta components. With PLSO, on the contrary, we can explicitly specify or learn the parameters. Fig. 4(c-d) demonstrates that PLSO is able to delineate the slow/theta components without any discontinuity.

## 6.3 EEG data from the human brain under propofol anesthesia

We apply PLSO to the EEG data from a subject anesthetized with propofol anesthetic drug, to assess whether PLSO can leverage regularization to recover smooth spectral dynamics, which is widely-observed during propofol-induced unconsciousness [Purdon et al., 2013]. The data last  $T = 2,300$  seconds, sampled at  $f_s = 250$  Hz. The drug infusion starts at  $t = 0$  and the subject loses consciousness around  $t = 260$  seconds. We use  $J = 6$  and assume a 4-second PS interval.

**Smooth spectrogram** Fig. 5(a-b) shows a segment of the PLSO-estimated spectrogram with  $\lambda = 0$  and  $\lambda = \lambda_{CV}$ . They identify strong slow ( $0.1 \sim 2$  Hz) and alpha oscillations ( $8 \sim 15$  Hz), both well-known signatures of propofol-

<sup>1</sup>We use channel 1 of mouse ec013.528 for the LFP. The population spikes were simultaneously recorded.

<sup>2</sup>The details for TVAR is in the **Appendix J**.

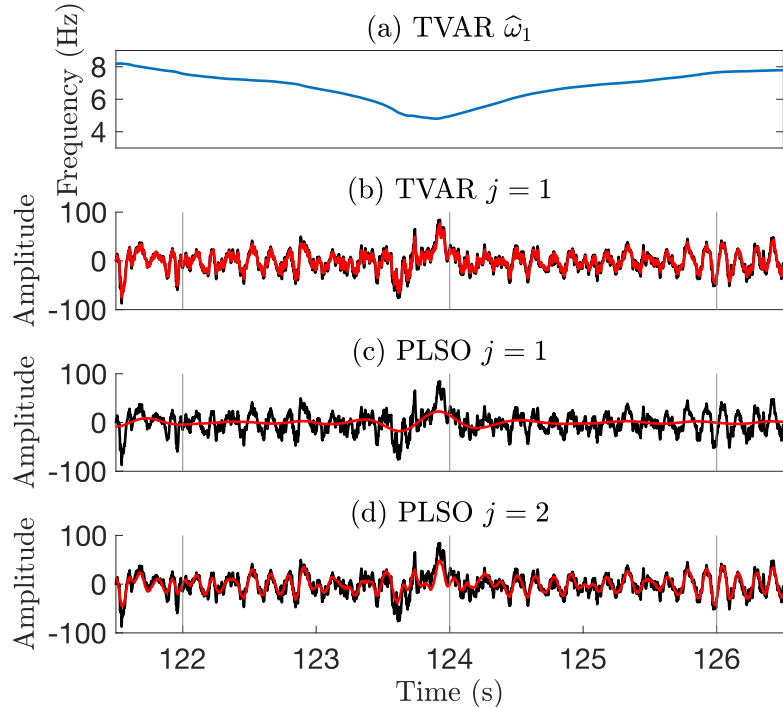


Figure 4: Hippocampus data. (a) time-varying  $\widehat{\omega}_1$  for TVAR. (b-d) Inferred mean trajectory (red) for (b) TVAR  $j = 1$ , (c) PLSO  $j = 1$ , and (d) PLSO  $j = 2$ , with raw data (black).

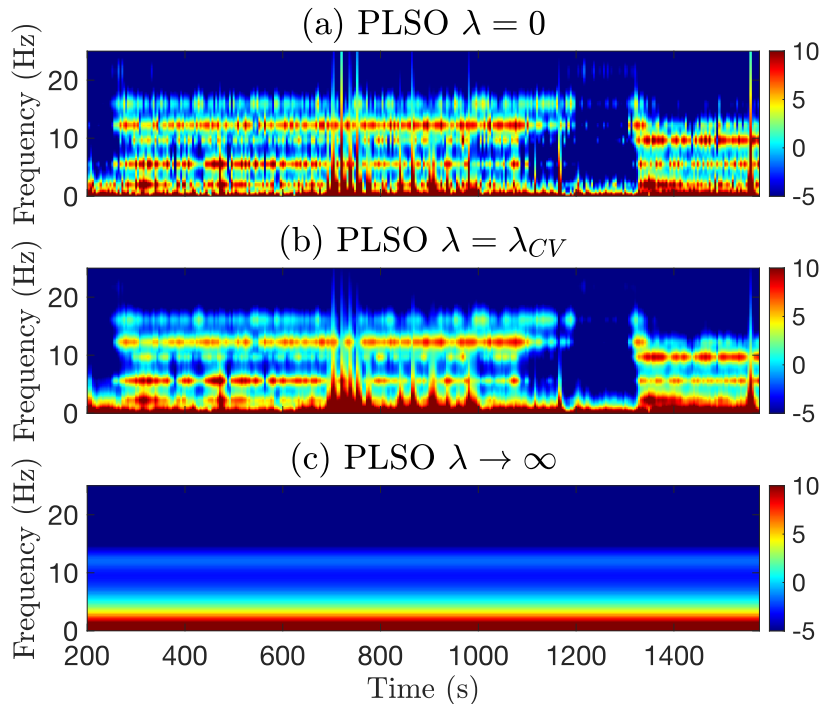


Figure 5: Spectrogram (in dB) under propofol anesthesia. PLSO with (a)  $\lambda = 0$  (b)  $\lambda = \lambda_{CV}$  (c)  $\lambda \rightarrow \infty$ .

induced unconsciousness. We also observe that the alpha band power diminishes between 1,200 and 1,350 seconds, suggesting that the subject regained consciousness before becoming unconscious again. PLSO with  $\lambda = 0$  exhibits PSD fluctuation across windows, since  $\{\sigma_{j,m}^2\}_{j,m}$  are estimated independently. The stationary PLSO ( $\lambda \rightarrow \infty$ ) is restrictive and fails to capture spectral dynamics (Fig. 5(c)). In contrast, PLSO with  $\lambda_{CV}$  exhibits smooth dynamics by pooling together estimates from the neighboring windows. The regularization also helps remove movement-related artifacts, shown as vertical lines in Fig. 5(a), around  $700 \sim 800/1,200$  seconds, and spurious power in  $20 \sim 25$  Hz band. In summary, PLSO with regularization enables smooth spectral dynamics estimation and spurious noise removal.

## 7 Conclusion

We presented the Piecewise Locally Stationary Oscillatory (PLSO) framework to model nonstationary time-series data with slowly time-varying spectra, as the superposition of piecewise stationary (PS) oscillatory components. PLSO strikes a balance between stochastic continuity of the data across PS intervals and stationarity within each interval. For inference, we introduce an algorithm that combines Kalman theory and nonconvex optimization algorithms. Applications to simulated/real data show that PLSO preserves time-domain continuity and captures time-varying spectra. Future directions include 1) the automatic identification of PS intervals and 2) the expansion to higher-order autoregressive models and diverse priors on the parameters that enforce continuity across intervals.

## References

[Adak, 1998] Adak, S. (1998). Time-dependent spectral analysis of nonstationary time series. *Journal of the American Statistical Association*, 93(444):1488–1501.

[Akaike, 1981] Akaike, H. (1981). Likelihood of a model and information criteria. *Journal of Econometrics*, 16(1):3–14.

[Ba et al., 2014] Ba, D., Babadi, B., Purdon, P. L., and Brown, E. N. (2014). Robust spectrotemporal decomposition by iteratively reweighted least squares. *Proceedings of the National Academy of Sciences*, 111(50):E5336–E5345.

[Barzilai and Borwein, 1988] Barzilai, J. and Borwein, J. M. (1988). Two-Point Step Size Gradient Methods. *IMA Journal of Numerical Analysis*, 8(1):141–148.

[Beck et al., 2018] Beck, A. M., Stephen, E. P., and Purdon, P. L. (2018). State space oscillator models for neural data analysis. In *2018 40th Annual International Conference of the IEEE Engineering in Medicine and Biology Society (EMBC)*, pages 4740–4743.

[Carter and Kohn, 1994] Carter, C. K. and Kohn, R. (1994). On gibbs sampling for state space models. *Biometrika*, 81(3):541–553.

[Cemgil and Godsill, 2005] Cemgil, A. T. and Godsill, S. J. (2005). Probabilistic phase vocoder and its application to interpolation of missing values in audio signals. In *2005 13th European Signal Processing Conference*, pages 1–4.

[Dahlhaus, 1997] Dahlhaus, R. (1997). Fitting time series models to nonstationary processes. *Ann. Statist.*, 25(1):1–37.

[Daubechies et al., 2011] Daubechies, I., Lu, J., and Wu, H.-T. (2011). Synchrosqueezed wavelet transforms: An empirical mode decomposition-like tool. *Applied and Computational Harmonic Analysis*, 30(2):243 – 261.

[Gramacy and Lee, 2008] Gramacy, R. B. and Lee, H. K. H. (2008). Bayesian treed gaussian process models with an application to computer modeling. *Journal of the American Statistical Association*, 103(483):1119–1130.

[Griffin and Jae Lim, 1984] Griffin, D. and Jae Lim (1984). Signal estimation from modified short-time fourier transform. *IEEE Transactions on Acoustics, Speech, and Signal Processing*, 32(2):236–243.

[Huang et al., 1998] Huang, N. E., Shen, Z., Long, S. R., Wu, M. C., Shih, H. H., Zheng, Q., Yen, N.-C., Tung, C. C., and Liu, H. H. (1998). The empirical mode decomposition and the hilbert spectrum for nonlinear and non-stationary time series analysis. *Proceedings of the Royal Society of London. Series A: Mathematical, Physical and Engineering Sciences*, 454(1971):903–995.

[Itakura and Saito, 1970] Itakura, F. and Saito, S. (1970). A statistical method for estimation of speech spectral density and formant frequencies.

[Kalman, 1960] Kalman, R. (1960). A new approach to linear filtering and prediction problems. *Journal of Basic Engineering*.

[Kim et al., 2018] Kim, S.-E., Behr, M. K., Ba, D., and Brown, E. N. (2018). State-space multitaper time-frequency analysis. *Proceedings of the National Academy of Sciences*, 115(1):E5–E14.

[Kitagawa and Gersch, 1985] Kitagawa, G. and Gersch, W. (1985). A smoothness priors time-varying ar coefficient modeling of nonstationary covariance time series. *IEEE Transactions on Automatic Control*, 30(1):48–56.

[Li and Lin, 2015] Li, H. and Lin, Z. (2015). Accelerated proximal gradient methods for nonconvex programming. In *Advances in Neural Information Processing Systems 28*, pages 379–387. Curran Associates, Inc.

[Lindsten and Schön, 2013] Lindsten, F. and Schön, T. B. (2013). *Backward Simulation Methods for Monte Carlo Statistical Inference*.

[Matsuda and Komaki, 2017] Matsuda, T. and Komaki, F. (2017). Time series decomposition into oscillation components and phase estimation. *Neural Computation*, 29(2):332–367.

[Mizuseki et al., 2009] Mizuseki, K., Sirota, A., Pastalkova, E., and Buzsaki, G. (2009). Theta oscillations provide temporal windows for local circuit computation in the entorhinal-hippocampal loop. *Neuron*, 64:267–280.

[Oppenheim et al., 2009] Oppenheim, A. V., Schafer, R. W., and Buck, J. R. (2009). *Discrete-time Signal Processing (3rd Ed.)*. Prentice-Hall, Inc.

[Priestley, 1965] Priestley, M. B. (1965). Evolutionary spectra and non-stationary processes. *Journal of the Royal Statistical Society. Series B (Methodological)*, 27(2):204–237.

[Purdon et al., 2013] Purdon, P. L., Pierce, E. T., Mukamel, E. A., Prerau, M. J., Walsh, J. L., Wong, K. F. K., Salazar-Gomez, A. F., Harrell, P. G., Sampson, A. L., Cimenser, A., Ching, S., Kopell, N. J., Tavares-Stoeckel, C., Habeeb, K., Merhar, R., and Brown, E. N. (2013). Electroencephalogram signatures of loss and recovery of consciousness from propofol. 110(12):E1142–E1151.

[Qi et al., 2002] Qi, Y., Minka, T. P., and Picard, R. W. (2002). Bayesian spectrum estimation of unevenly sampled nonstationary data. In *2002 IEEE International Conference on Acoustics, Speech, and Signal Processing*, volume 2, pages II–1473–II–1476.

[Rasmussen and Williams, 2005] Rasmussen, C. E. and Williams, C. K. I. (2005). *Gaussian Processes for Machine Learning (Adaptive Computation and Machine Learning)*. The MIT Press.

[Rosen et al., 2009] Rosen, O., Stoffer, D. S., and Wood, S. (2009). Local spectral analysis via a bayesian mixture of smoothing splines. *Journal of the American Statistical Association*, 104(485):249–262.

[Solin et al., 2018] Solin, A., Hensman, J., and Turner, R. E. (2018). Infinite-horizon gaussian processes. In *Advances in Neural Information Processing Systems 31*, pages 3486–3495.

[Solin and Särkkä, 2014] Solin, A. and Särkkä, S. (2014). Explicit Link Between Periodic Covariance Functions and State Space Models. In *Proceedings of the Seventeenth International Conference on Artificial Intelligence and Statistics*, volume 33 of *Proceedings of Machine Learning Research*, pages 904–912. PMLR.

[Song et al., 2018] Song, A. H., Chakravarty, S., and Brown, E. N. (2018). A smoother state space multitaper spectrogram. In *2018 40th Annual International Conference of the IEEE Engineering in Medicine and Biology Society (EMBC)*, pages 33–36.

[Soulat et al., 2019] Soulat, H., Stephen, E. P., Beck, A. M., and Purdon, P. L. (2019). State space methods for phase amplitude coupling analysis. *bioRxiv*.

[Turner and Sahani, 2014] Turner, R. E. and Sahani, M. (2014). Time-frequency analysis as probabilistic inference. *IEEE Transactions on Signal Processing*, 62(23):6171–6183.

[West et al., 1999] West, M., Prado, R., and Krystal, A. D. (1999). Evaluation and comparison of eeg traces: Latent structure in nonstationary time series. *Journal of the American Statistical Association*, 94(448):1083–1095.

[Whittle, 1953] Whittle, P. (1953). Estimation and information in stationary time series. *Ark. Mat.*, 2(5):423–434.

[Wilkinson et al., 2019] Wilkinson, W. J., Riis Andersen, M., Reiss, J. D., Stowell, D., and Solin, A. (2019). Unifying probabilistic models for time-frequency analysis. In *2019 IEEE International Conference on Acoustics, Speech and Signal Processing (ICASSP)*, pages 3352–3356.

[Wilson and Adams, 2013] Wilson, A. G. and Adams, R. P. (2013). Gaussian process kernels for pattern discovery and extrapolation. In *Proceedings of the 30th International Conference on International Conference on Machine Learning - Volume 28*, ICML’13, page III–1067–III–1075.

[Wilson et al., 2008] Wilson, K. W., Raj, B., Smaragdis, P., and Divakaran, A. (2008). Speech denoising using non-negative matrix factorization with priors. In *2008 IEEE International Conference on Acoustics, Speech and Signal Processing*, pages 4029–4032.

[Wright, 2015] Wright, S. J. (2015). Coordinate descent algorithms. *Mathematical Programming*, 151:3–34.

## Appendix

References to the sections in the section headings are made with respect to the sections in the main text.

Below is the table of contents for the Appendix.

- A. Continuous model interpretation of PLSO (*Section 3*)
- B. Proof for Proposition 1 (*Section 3.2.1*)
- C. Proof for Proposition 2 (*Section 3.2.2*)
- D. Initialization for PLSO (*Section 4*)
- E. Optimization for  $\{\sigma_{j,m}^2\}_{j,m}$  via proximal gradient update (*Section 4.1.1*)
- F. Lipschitz constant for  $\nabla f(\{\sigma_{j,m}^2\}_{j,m}; \theta)$  (*Section 4.1.1*)
- G. Inference with  $p(\{\mathbf{z}_j\}_j \mid \{\sigma_{j,m}^2\}_{j,m}, \mathbf{y}, \theta)$  (*Section 4.2*)
- H. Computational efficiency of PLSO vs. GP-PS
- I. Simulation experiment (*Section 5.1*)
- J. Details of TVAR model (*Section 5.2*)
- K. Anesthesia EEG dataset (*Section 5.3*)

## A. Continuous model interpretation of PLSO

We can establish the equivalent continuous model of the PLSO in Eq. 2, using stochastic different equation

$$\frac{d\tilde{z}_j(t)}{dt} = \underbrace{\left( \left( -\frac{1}{l_j} \right) \oplus \begin{pmatrix} 0 & -\omega_j \\ \omega_j & 0 \end{pmatrix} \right)}_{\mathbf{F}} \tilde{z}_j(t) + \varepsilon(t), \quad (11)$$

where  $\tilde{z}_j(t) : \mathbb{R} \rightarrow \mathbb{R}^2$ ,  $\oplus$  denotes the Kronecker sum and  $\varepsilon(t) \sim \mathcal{N}(0, \sigma_j^2 \mathbf{I}_{2 \times 2})$ . Discretizing the solution of Eq. 11 at  $\Delta$ , such that  $\tilde{\mathbf{z}}_{j,k} = \tilde{z}_j(k\Delta)$ , yields Eq. 2. Consequently, we obtain the following for  $\Delta > 0$

$$\begin{aligned} \exp(\mathbf{F}\Delta) &= \exp(-\Delta/l_j) \mathbf{R}(\omega_j), \\ \sigma_j^2 \int_0^\Delta \exp(\mathbf{F}(\Delta - \tau)) \exp(\mathbf{F}(\Delta - \tau))^T d\tau &= \sigma_j^2 (1 - \exp(-2\Delta/l_j)) \mathbf{I}_{2 \times 2}. \end{aligned} \quad (12)$$

This interpretation also extends to the nonstationary PLSO case. The corresponding continuous model for  $\tilde{\mathbf{z}}_{j,mN+n}$  in Eq. 3 is the same as Eq. 11, with different variance  $\mathbb{E}[\varepsilon_j(t)\varepsilon_j^T(t)] = \sum_{m=1}^M \sigma_{j,m}^2 \cdot \mathbf{1}((\frac{m-1}{M})T \leq t < (\frac{m}{M})T) \mathbf{I}_{2 \times 2}$ .

## B. Proof for Proposition 1 (*Section 3.2.1*)

**Proposition 1.** For a given  $m$ , as  $\Delta \rightarrow 0$ , the samples on either side of the interval boundary, which are  $\tilde{\mathbf{z}}_{j,(m+1)N}$  and  $\tilde{\mathbf{z}}_{j,(m+1)N+1}$ , become equivalent,

$$\lim_{\Delta \rightarrow 0} \tilde{\mathbf{z}}_{j,(m+1)N} = \lim_{\Delta \rightarrow 0} \tilde{\mathbf{z}}_{j,(m+1)N+1}.$$

*Proof.* To analyze Eq. 3 in the limit of  $\Delta \rightarrow 0$ , we use the equivalent continuous model (Eq. 12). It suffices to show that  $\lim_{\Delta \rightarrow 0} \exp(\mathbf{F}\Delta) = \mathbf{I}_{2 \times 2}$  and  $\lim_{\Delta \rightarrow 0} \mathbb{E}[\varepsilon_{j,(m+1)N+1}\varepsilon_{j,(m+1)N+1}^T] = \mathbf{0}$ . We have,

$$\begin{aligned} \lim_{\Delta \rightarrow 0} \exp(\mathbf{F}\Delta) &= \mathbf{I}_{2 \times 2} + \lim_{\Delta \rightarrow 0} \sum_{k=1}^{\infty} \frac{\Delta^k}{k!} \mathbf{F}^k = \mathbf{I}_{2 \times 2} \\ \lim_{\Delta \rightarrow 0} \mathbb{E}[\varepsilon_{j,(m+1)N+1}\varepsilon_{j,(m+1)N+1}^T] / \sigma_{j,m+1}^2 &= \lim_{\Delta \rightarrow 0} \int_0^\Delta \exp(\mathbf{F}(\Delta - \tau)) \exp(\mathbf{F}(\Delta - \tau))^T d\tau = \mathbf{0}. \end{aligned}$$

□

## C. Proof for Proposition 2 (*Section 3.2.2*)

**Proposition 2.** Assume  $l_j \ll N\Delta$ , such that  $\mathbf{P}_{m,N}^j = \mathbf{P}_{m,\infty}^j$ . In Eq. 3, the difference between  $\mathbf{P}_{m,\infty}^j = \sigma_{j,m}^2 \mathbf{I}_{2 \times 2}$  and  $\mathbf{P}_{m+1,\infty}^j = \sigma_{j,m+1}^2 \mathbf{I}_{2 \times 2}$  decays exponentially fast as a function of  $n$ , for  $1 \leq n \leq N$ ,

$$\mathbf{P}_{m+1,n}^j = \mathbf{P}_{m+1,\infty}^j + \exp(-2n\Delta/l_j) (\mathbf{P}_{m,\infty}^j - \mathbf{P}_{m+1,\infty}^j).$$

*Proof.* We first obtain the steady-state covariance  $\mathbf{P}_{m,\infty}^j$ . Since we assume  $\mathbf{P}_{1,1}^j = \sigma_{j,1}^2 \mathbf{I}_{2 \times 2}$ , we can show that  $\forall m, n$ ,  $\mathbf{P}_{m,n}^j$  is a diagonal matrix, noting that  $\mathbf{R}(\omega_j) \mathbf{R}^T(\omega_j) = \mathbf{I}_{2 \times 2}$ . Denoting  $\mathbf{P}_{m,\infty}^j = \alpha \mathbf{I}_{2 \times 2}$ , we now use the discrete Lyapunov equation

$$\begin{aligned} \mathbf{P}_{m,\infty}^j &= \exp(-2\Delta/l_j) \mathbf{R}(\omega_j) \mathbf{P}_{m,\infty}^j \mathbf{R}^T(\omega_j) \\ &\quad + \sigma_{j,m}^2 (1 - \exp(-2\Delta/l_j)) \mathbf{I}_{2 \times 2} \\ &\Rightarrow \alpha = \exp(-2\Delta/l_j) \alpha + \sigma_{j,m}^2 (1 - \exp(-2\Delta/l_j)) \\ &\Rightarrow \mathbf{P}_{m,\infty}^j = \sigma_{j,m}^2 \mathbf{I}_{2 \times 2}. \end{aligned} \quad (13)$$

We now prove the proposition by induction. For fixed  $j$  and  $m$ , and for  $n = 1$ ,

$$\begin{aligned} \mathbf{P}_{m+1,1}^j &= \exp(-2\Delta/l_j) \mathbf{R}(\omega_j) \mathbf{P}_{m,N}^j \mathbf{R}^T(\omega_j) \\ &\quad + \sigma_{j,m+1}^2 (1 - \exp(-2\Delta/l_j)) \mathbf{I}_{2 \times 2} \\ &= \{\sigma_{j,m+1}^2 + \exp(-2\Delta/l_j) (\sigma_{j,m}^2 - \sigma_{j,m+1}^2)\} \mathbf{I}_{2 \times 2}. \end{aligned}$$

Assuming the same holds for  $n = n' - 1$ , we have for  $n = n'$ ,

$$\begin{aligned} \mathbf{P}_{m+1,n'}^j &= \exp(-2\Delta/l_j) \mathbf{R}(\omega_j) \mathbf{P}_{m,n'-1}^j \mathbf{R}^T(\omega_j) \\ &\quad + \sigma_{j,m+1}^2 (1 - \exp(-2\Delta/l_j)) \mathbf{I}_{2 \times 2} \\ &= \exp(-2\Delta/l_j) \sigma_{j,m+1}^2 \mathbf{I}_{2 \times 2} \\ &\quad + \exp(-2n'\Delta/l_j) (\sigma_{j,m}^2 - \sigma_{j,m+1}^2) \mathbf{I}_{2 \times 2} \\ &\quad + \sigma_{j,m+1}^2 (1 - \exp(-2\Delta/l_j)) \mathbf{I}_{2 \times 2} \\ &= \{\sigma_{j,m+1}^2 + \exp(-2n'\Delta/l_j) (\sigma_{j,m}^2 - \sigma_{j,m+1}^2)\} \mathbf{I}_{2 \times 2}. \end{aligned}$$

By the principle of induction, Eq. 7 holds for  $1 \leq n \leq N$ .  $\square$

## D. Initialization & Estimation for PLSO (*Section 4*)

### D.1 Initialization

As noted in the main text, we use AIC to determine the optimal number of  $J$ . For a given number of components  $J$ , we first construct the spectrogram of the data using STFT and identify the frequency bands with prominent power, i.e., frequency bands whose average power exceeds pre-determined threshold. The center frequencies of these bands serve as the initial center frequencies  $\{\omega_j^{\text{init}}\}_j$ , which are either fixed throughout the algorithm or further refined through the estimation algorithm in the main text. If  $J$  exceeds the number of identified frequency bands from the spectrogram, 1) we first place  $\{\omega_j^{\text{init}}\}_j$  in the prominent frequency bands and 2) we then place the remaining components uniformly spread out in  $[0, \omega_c]$ , where  $\omega_c$  is a cutoff frequency to be further determined in the next section. As for  $\{l_j^{\text{init}}\}_j$ , we set it to be a certain fraction of the corresponding  $\{\omega_j^{\text{init}}\}_j$ . We then fit  $\{\sigma_{j,m}^2\}_{j,m}$  and  $\theta$  with  $\lambda = 0$ , through the procedure explained in Stage 1. We finally use these estimates as initial values for other values of  $\lambda$ .

### D.2 Estimation for $\sigma_\nu^2$

There are two possible ways to estimate the observation noise variance  $\sigma_\nu^2$ . The first approach is to perform maximum likelihood estimation of  $f(\{\sigma_{j,m}^2\}_{j,m}; \theta)$  with respect to  $\sigma_\nu^2$ . The second approach, which we found to work *better* in practice and use throughout the manuscript, is to directly estimate it from the Fourier transform of the data. Given a cutoff frequency  $\omega_c$ , informed by domain knowledge, we take the average power of the Fourier transform of  $\mathbf{y}$  in  $[\omega_c, f_s/2]$ . For instance, it is widely known that the spectral content below 40 Hz in anesthesia EEG dataset is physiologically relevant and we use  $\omega_c \simeq 40$  Hz.

## E. Optimization for $\{\sigma_{j,m}^2\}_{j,m}$ via proximal gradient update (*Section 4.1.1*)

We discuss the algorithm to obtain a local optimal solution of  $\{\sigma_{j,m}^2\}_{j,m}$  to the MAP optimization problem in Eq. 8. We define  $\psi_{j,m} = \log \sigma_{j,m}^2$  and  $\Psi = [\psi_{1,1}, \dots, \psi_{1,M}, \dots, \psi_{J,M}] \in \mathbb{R}^{JM}$  for notational decluttering, to be used in this section.

We rewrite Eq. 8 as

$$\begin{aligned} &\min_{\Psi} \underbrace{-\log p(\Psi | \mathbf{y}, \theta)}_{h(\Psi; \theta)} \\ &= \min_{\Psi} \underbrace{\frac{1}{2} \sum_{m=1}^M \sum_{n=1}^N \left\{ \log \gamma^{(m)}(\omega_n) + \frac{I^{(m)}(\omega_n)}{\gamma^{(m)}(\omega_n)} \right\}}_{-f(\Psi; \theta)} \\ &\quad + \underbrace{\frac{\lambda}{2} \sum_{j=1}^J \sum_{m=1}^M (\psi_{j,m} - \psi_{j,m-1})^2}_{-g(\Psi; \theta)} \\ &= \min_{\Psi} -f(\Psi; \theta) - g(\Psi; \theta). \end{aligned} \quad (14)$$

The algorithm is described in Algorithm 1. It follows the steps outlined in the inexact accelerated proximal gradient algorithm [Li and Lin, 2015]. For faster convergence, we use larger step sizes with the Barzilai-Borwein (BB) step size

initialization rule [Barzilai and Borwein, 1988]. For rest of this section, we drop dependence on  $\theta$ . The main novelty of our algorithm is the proximal gradient update

$$\begin{aligned}
& \mathbf{u}^{(l+1)} \\
&= \text{prox}_{-\alpha_{\mathbf{w}}^{(l)} g}(\mathbf{w}^{(l)} + \alpha_{\mathbf{w}}^{(l)} \nabla f(\mathbf{w}^{(l)})) \\
&= \arg \min_{\Psi} \frac{1}{2\alpha_{\mathbf{w}}^{(l)}} \|\Psi - (\mathbf{w}^{(l)} + \alpha_{\mathbf{w}}^{(l)} \nabla f(\mathbf{w}^{(l)}))\|^2 - g(\Psi) \\
&= \arg \min_{\Psi} \sum_{j=1}^J \sum_{m=1}^M \frac{\left( \left( \mathbf{w}_{j,m}^{(l)} + \alpha_{\mathbf{w}}^{(l)} \cdot \frac{\partial f(\mathbf{w}^{(l)})}{\partial \mathbf{w}_{j,m}} \right) - \psi_{j,m} \right)^2}{2\alpha_{\mathbf{w}}^{(l)}} \\
&\quad + \frac{\lambda}{2} (\psi_{j,m} - \psi_{j,m-1})^2,
\end{aligned} \tag{15}$$

where the same holds for  $\mathbf{x}^{(l+1)} = \text{prox}_{-\alpha_{\Psi}^{(l)} g}(\Psi^{(l)} + \alpha_{\Psi}^{(l)} \nabla f(\Psi^{(l)}))$ . The auxiliary variables  $\mathbf{w}, \mathbf{u}, \mathbf{x} \in \mathbb{R}^{JM}$  ensure convergence of  $\Psi$ . We use  $\mathbf{w}_{j,m}^{(l)}$  to denote  $((m-1)J+j)^{\text{th}}$  entry of  $\mathbf{w}^{(l)}$ . As mentioned in the main text, this can be solved in a computationally efficient manner by using Kalman filter/smooth.

---

**Algorithm 1:** Inference for  $\Psi$  via inexact APG

---

**Result:**  $\hat{\Psi}$   
**Initialize**  $\Psi^{(0)} = \Psi^{(1)} = \mathbf{u}^{(1)}$ ,  $\beta^{(0)} = 0$ ,  $\beta^{(1)} = 1$ ,  $\delta > 0$ ,  $\rho < 1$   
**for**  $l \leftarrow 1$  **to**  $L$  **do**  
 $\mathbf{w}^{(l)} = \Psi^{(l)} + \frac{\beta^{(l-1)}}{\beta^{(l)}} (\mathbf{u}^{(l)} - \Psi^{(l)}) + \frac{\beta^{(l-1)} - 1}{\beta^{(l)}} (\Psi^{(l)} - \Psi^{(l-1)})$   
**(BB step size initialization rule)**  
 $\mathbf{s}^{(l)} = \mathbf{u}^{(l)} - \mathbf{w}^{(l-1)}$ ,  $\mathbf{r}^{(l)} = -\nabla f(\mathbf{u}^{(l)}) + \nabla f(\mathbf{w}^{(l-1)})$   
 $\alpha_{\mathbf{w}}^{(l)} = ((\mathbf{s}^{(l)})^T \mathbf{s}^{(l)}) / ((\mathbf{s}^{(l)})^T \mathbf{r}^{(l)})$   
 $\mathbf{s}^{(l)} = \mathbf{x}^{(l)} - \Psi^{(l-1)}$ ,  $\mathbf{r}^{(l)} = -\nabla f(\mathbf{x}^{(l)}) + \nabla f(\Psi^{(l-1)})$   
 $\alpha_{\Psi}^{(l)} = ((\mathbf{s}^{(l)})^T \mathbf{s}^{(l)}) / ((\mathbf{s}^{(l)})^T \mathbf{r}^{(l)})$   
**(Proximal update step)**  
**repeat**  
 $\mathbf{u}^{(l+1)} = \text{prox}_{-\alpha_{\mathbf{w}}^{(l)} g}(\mathbf{w}^{(l)} + \alpha_{\mathbf{w}}^{(l)} \nabla f(\mathbf{w}^{(l)}))$   
 $\alpha_{\mathbf{w}}^{(l)} = \rho \cdot \alpha_{\mathbf{w}}^{(l)}$   
**until**  $h(\mathbf{u}^{(l+1)}) \leq h(\mathbf{w}^{(l)}) - \delta \|\mathbf{u}^{(l+1)} - \mathbf{w}^{(l)}\|^2$ ;  
**repeat**  
 $\mathbf{x}^{(l+1)} = \text{prox}_{-\alpha_{\Psi}^{(l)} g}(\Psi^{(l)} + \alpha_{\Psi}^{(l)} \nabla f(\Psi^{(l)}))$   
 $\alpha_{\Psi}^{(l)} = \rho \cdot \alpha_{\Psi}^{(l)}$   
**until**  $h(\mathbf{x}^{(l+1)}) \leq h(\Psi^{(l)}) - \delta \|\mathbf{x}^{(l+1)} - \Psi^{(l)}\|^2$ ;  
 $\beta^{(l+1)} = \frac{1 + \sqrt{4(\beta^{(l)})^2 + 1}}{2}$   
 $\Psi^{(l+1)} = \begin{cases} \mathbf{u}^{(l+1)} & \text{if } h(\mathbf{u}^{(l+1)}) \leq h(\mathbf{x}^{(l+1)}) \\ \mathbf{x}^{(l+1)} & \text{otherwise} \end{cases}$   
**end**  
 $\hat{\Psi} = \Psi^{(L)}$

---

## F. Lipschitz constant for $\nabla f(\{\sigma_{j,m}^2\}_{j,m}; \theta)$ (Section 4.1.1)

In this section, we prove that under some assumptions, we can show that the log-likelihood  $f(\{\sigma_{j,m}^2\}_{j,m}; \theta)$  has Lipschitz continuous gradient with the Lipschitz constant  $C$ . As in the previous section, we use  $\psi_{j,m} = \log \sigma_{j,m}^2$  and  $\Psi = [\psi_{1,1}, \dots, \psi_{1,M}, \dots, \psi_{J,M}] \in \mathbb{R}^{JM}$ .

Let us start by restating the definition of Lipschitz continuous gradient.

**Definition** A continuously differentiable function  $f: \mathcal{S} \rightarrow \mathbb{R}$  is Lipschitz continuous gradient if

$$\|\nabla f(\mathbf{x}) - \nabla f(\mathbf{y})\|_2 \leq C \|\mathbf{x} - \mathbf{y}\|_2 \quad \text{for every } \mathbf{x}, \mathbf{y} \in \mathcal{S}, \quad (16)$$

where  $\mathcal{S}$  is a compact subset of  $\mathbb{R}^{JM}$  and  $C > 0$  is the Lipschitz constant.

Our goal is to find the constant  $C$  for the Whittle likelihood  $f(\Psi; \theta)$

$$\begin{aligned} f(\Psi; \theta) &= -\frac{1}{2} \sum_{m=1}^M \sum_{n=1}^N \left\{ \log \gamma_{m,n} + \frac{I_{m,n}}{\gamma_{m,n}} \right\} \\ &= -\frac{1}{2} \underbrace{\sum_{m=1}^M \sum_{n=1}^N \log \left( \sigma_\nu^2 + \sum_{j=1}^J \exp(\psi_{j,m}) \alpha_{j,n} \right)}_{f_1(\Psi; \theta)} \\ &\quad - \underbrace{\frac{1}{2} \sum_{m=1}^M \sum_{n=1}^N \frac{I_{m,n}}{\left( \sigma_\nu^2 + \sum_{j=1}^J \exp(\psi_{j,m}) \alpha_{j,n} \right)}}_{f_2(\Psi; \theta)}, \end{aligned} \quad (17)$$

where we use  $\gamma_{m,n} = \gamma^{(m)}(\omega_n)$  and  $I_{m,n} = I^{(m)}(\omega_n)$  for notational simplicity and

$$\alpha_{j,n} = \frac{(1 - \exp(-2\Delta/l_j))}{1 + \exp(-2\Delta/l_j) - 2 \exp(-\Delta/l_j) \cos(\omega_n - \omega_j)}.$$

We make the following assumptions

1.  $I_{m,n}$  is bounded, i.e.,  $I_{m,n} \leq C_I$ . With the real-world signal, we can reasonably assume that  $I_{m,n}$  or energy of the signal is bounded.
2.  $\forall j, m$ ,  $\psi_{j,m}$  is bounded, i.e.,  $|\psi_{j,m}| \leq \log C_\psi$  for some  $C_\psi > 1$ . This implies  $1/C_\psi \leq \exp(\psi_{j,m}) \leq C_\psi$ .

In addition, we have the following facts

1.  $I_{m,n}, \alpha_{j,n}$ , and  $\gamma_{m,n}$  are nonnegative.
2.  $I_{m,n}$  and  $\gamma_{m,n}$  are bounded. This follows from the aforementioned assumptions.

3. For given  $\{l_j\}_j$ , we have bounded  $\alpha_{j,n}$ . To see this, note that the maximum of  $\alpha_{j,n}$  is achieved at  $\omega_n = \omega_j$ ,

$$\begin{aligned} \max \alpha_{j,n} &= \frac{(1 - \exp(-2\Delta/l_j))}{1 + \exp(-2\Delta/l_j) - 2 \exp(-\Delta/l_j)} \\ &= \frac{(1 + \exp(-\Delta/l_j))}{(1 - \exp(-\Delta/l_j))}. \end{aligned} \quad (18)$$

Therefore, denoting  $l_{\max} = \max_j \{l_j\}_j$ ,

$$\max \alpha_{j,n} \leq \frac{(1 + \exp(-\Delta/l_{\max}))}{(1 - \exp(-\Delta/l_{\max}))} = C_\alpha. \quad (19)$$

Finally, we define  $\mathcal{S} = [-\log C_\psi, \log C_\psi] \subset \mathbb{R}^{JM}$ .

We want to compute the Lipschitz constant for  $\nabla f_1(\Psi)$  and  $\nabla f_2(\Psi)$  for  $\Psi, \bar{\Psi} \in \mathcal{S}$ , i.e.,

$$\begin{cases} \|\nabla f_1(\Psi) - \nabla f_1(\bar{\Psi})\|_2 \leq C_1 \|\Psi - \bar{\Psi}\|_2 \\ \|\nabla f_2(\Psi) - \nabla f_2(\bar{\Psi})\|_2 \leq C_2 \|\Psi - \bar{\Psi}\|_2, \end{cases} \quad (20)$$

where we dropped dependence on  $\theta$  for notational simplicity. Consequently, the triangle inequality yields

$$\begin{aligned} &\|\nabla f(\Psi) - \nabla f(\bar{\Psi})\|_2 \\ &\leq \|\nabla f_1(\Psi) - \nabla f_1(\bar{\Psi})\|_2 + \|\nabla f_2(\Psi) - \nabla f_2(\bar{\Psi})\|_2 \\ &\leq (C_1 + C_2) \|\Psi - \bar{\Psi}\|_2. \end{aligned} \quad (21)$$

### Lipschitz constant $C_1$ for $\nabla f_1(\Psi)$

Let us examine  $f_1(\Psi)$  first. The derivative with respect to  $\psi_{j,m}$  is given as

$$\begin{aligned} \frac{\partial f_1(\Psi)}{\partial \psi_{j,m}} &= \sum_{n=1}^N \alpha_{j,n} \cdot \underbrace{\frac{\exp(\psi_{j,m})}{\sigma_\nu^2 + \sum_{j'=1}^J \exp(\psi_{j',m}) \alpha_{j',n}}}_{\tilde{f}(\psi_{j,m})} \\ &= \sum_{n=1}^N \alpha_{j,n} \tilde{f}(\psi_{j,m}). \end{aligned} \quad (22)$$

We now have

$$\left| \frac{\partial f_1(\Psi)}{\partial \psi_{j,m}} - \frac{\partial f_1(\bar{\Psi})}{\partial \psi_{j,m}} \right| = \sum_{n=1}^N |\alpha_{j,n}| \cdot \left| \tilde{f}(\psi_{j,m}) - \tilde{f}(\bar{\psi}_{j,m}) \right|. \quad (23)$$

Without loss of generality, we assume  $\psi_{j,m} \geq \bar{\psi}_{j,m}$ . We now apply the mean value theorem (MVT) to  $\tilde{f}(\psi_{j,m})$

$$\tilde{f}(\psi_{j,m}) - \tilde{f}(\bar{\psi}_{j,m}) = \tilde{f}'(\psi'_{j,m})(\psi_{j,m} - \bar{\psi}_{j,m}), \quad (24)$$

where  $\psi'_{j,m} \in [\bar{\psi}_{j,m}, \psi_{j,m}]$ . We can compute and bound  $\tilde{f}'(\psi'_{j,m}) = d\tilde{f}(\psi'_{j,m})/d\psi'_{j,m}$  as follows

$$\begin{aligned} \tilde{f}'(\psi'_{j,m}) &= \frac{\exp(\psi'_{j,m})}{\sigma_\nu^2 + \sum_{j'=1}^J \exp(\psi'_{j',m}) \alpha_{j',n}} \\ &\quad - \frac{\alpha_{j,n} \exp^2(\psi'_{j,m})}{(\sigma_\nu^2 + \sum_{j'=1}^J \exp(\psi'_{j',m}) \alpha_{j',n})^2} \\ &= \frac{\exp(\psi'_{j,m})}{\sigma_\nu^2 + \sum_{j'=1}^J \exp(\psi'_{j',m}) \alpha_{j',n}} \\ &\quad \times \underbrace{\left(1 - \frac{\alpha_{j,n} \exp(\psi'_{j,m})}{\sigma_\nu^2 + \sum_{j'=1}^J \exp(\psi'_{j',m}) \alpha_{j',n}}\right)}_{\leq 1} \\ &\leq \frac{\exp(\psi'_{j,m})}{\sigma_\nu^2 + \sum_{j'=1}^J \exp(\psi'_{j',m}) \alpha_{j',n}} \\ &\leq \frac{C_\psi}{\sigma_\nu^2}. \end{aligned} \quad (25)$$

Combining Eq. 24 and 25, we have

$$\begin{aligned} &\sum_{n=1}^N |\alpha_{j,n}| \cdot \left| \tilde{f}(\psi_{j,m}) - \tilde{f}(\bar{\psi}_{j,m}) \right| \\ &= \sum_{n=1}^N |\alpha_{j,n}| \cdot \left| \tilde{f}'(\psi'_{j,m})(\psi_{j,m} - \bar{\psi}_{j,m}) \right| \\ &\leq \frac{NC_\alpha C_\psi}{\sigma_\nu^2} |\psi_{j,m} - \bar{\psi}_{j,m}|. \end{aligned} \quad (26)$$

We thus have,

$$\begin{aligned} \|\nabla f_1(\Psi) - \nabla f_1(\bar{\Psi})\|_2^2 &= \sum_{j=1}^J \sum_{m=1}^M \left( \frac{\partial f_1(\Psi)}{\partial \psi_{j,m}} - \frac{\partial f_1(\bar{\Psi})}{\partial \psi_{j,m}} \right)^2 \\ &\leq \left( \frac{JMNC_\alpha C_\psi}{\sigma_\nu^2} \right)^2 \|\Psi - \bar{\Psi}\|_2^2. \end{aligned} \quad (27)$$

### Lipschitz constant $C_2$ for $\nabla f_2(\Psi)$

Computing  $C_2$  proceeds in a similar manner to computing  $C_1$ . The derivative with respect to  $\psi_{j,m}$  is given as

$$\frac{\partial f_2(\Psi)}{\partial \psi_{j,m}} = - \sum_{n=1}^N I_{m,n} \alpha_{j,n} \cdot \underbrace{\frac{\exp(\psi_{j,m})}{(\sigma_\nu^2 + \sum_{j'=1}^J \exp(\psi'_{j',m}) \alpha_{j',n})^2}}_{\tilde{f}(\psi_{j,m})}. \quad (28)$$

We now have

$$\left| \frac{\partial f_2(\Psi)}{\partial \psi_{j,m}} - \frac{\partial f_2(\bar{\Psi})}{\partial \psi_{j,m}} \right| = \sum_{n=1}^N |I_{m,n} \alpha_{j,n}| \cdot \left| -\tilde{f}(\psi_{j,m}) + \tilde{f}(\bar{\psi}_{j,m}) \right|. \quad (29)$$

Without loss of generality, assume  $\psi_{j,m} \geq \bar{\psi}_{j,m}$ . To apply MVT, we need to compute and bound  $\tilde{f}'(\psi'_{j,m})$

$$\begin{aligned} \tilde{f}'(\psi'_{j,m}) &= \frac{\exp(\psi'_{j,m})}{(\sigma_\nu^2 + \sum_{j'=1}^J \exp(\psi'_{j',m}) \alpha_{j',n})^2} \\ &\quad - \frac{2\alpha_{j,n} \exp^2(\psi'_{j,m})}{(\sigma_\nu^2 + \sum_{j'=1}^J \exp(\psi'_{j',m}) \alpha_{j',n})^3} \\ &= \frac{\exp(\psi'_{j,m})}{(\sigma_\nu^2 + \sum_{j'=1}^J \exp(\psi'_{j',m}) \alpha_{j',n})^2} \\ &\quad \times \underbrace{\left(1 - \frac{2\alpha_{j,n} \exp(\psi'_{j,m})}{\sigma_\nu^2 + \sum_{j'=1}^J \exp(\psi'_{j',m}) \alpha_{j',n}}\right)}_{\leq 1} \\ &\leq \frac{\exp(\psi'_{j,m})}{(\sigma_\nu^2 + \sum_{j'=1}^J \exp(\psi'_{j',m}) \alpha_{j',n})^2} \\ &\leq \frac{C_\psi}{\sigma_\nu^4}. \end{aligned} \quad (30)$$

Applying MVT,

$$\begin{aligned}
& \sum_{n=1}^N |I_{m,n} \alpha_{j,n}| \cdot \left| -\tilde{f}(\psi_{j,m}) + \tilde{f}(\bar{\psi}_{j,m}) \right| \\
&= \sum_{n=1}^N |I_{m,n} \alpha_{j,n}| \cdot \left| \tilde{f}'(\psi'_{j,m})(\psi_{j,m} - \bar{\psi}_{j,m}) \right| \\
&\leq \frac{NC_I C_\alpha C_\psi}{\sigma_\nu^4} |\psi_{j,m} - \bar{\psi}_{j,m}|.
\end{aligned} \tag{31}$$

We thus have,

$$\begin{aligned}
& \|\nabla f_2(\Psi) - \nabla f_2(\bar{\Psi})\|_2^2 \\
&= \sum_{j=1}^J \sum_{m=1}^M \left( \frac{\partial f_2(\Psi)}{\partial \psi_{j,m}} - \frac{\partial f_2(\bar{\Psi})}{\partial \psi_{j,m}} \right)^2 \\
&\leq \left( \frac{JMN C_\alpha C_\psi C_I}{\sigma_\nu^4} \right)^2 \|\Psi - \bar{\Psi}\|_2^2.
\end{aligned} \tag{32}$$

Collecting the Lipschitz constants  $C_1$  and  $C_2$ , we finally have

$$\|\nabla f(\Psi) - \nabla f(\bar{\Psi})\|_2 \leq \underbrace{\frac{JMN C_\alpha C_\psi}{\sigma_\nu^2} \left( 1 + \frac{C_I}{\sigma_\nu^2} \right)}_C \|\Psi - \bar{\Psi}\|_2. \tag{33}$$

## G. Inference with $p\left(\{\mathbf{z}_j\}_j \mid \{\sigma_{j,m}^2\}_{j,m}, \mathbf{y}, \theta\right)$ (Section 4.2)

We present the details for performing inference with the *sample-level* posterior,  $p(\{\mathbf{z}_j\}_j \mid \{\hat{\sigma}_{j,m}^2\}_{j,m}, \mathbf{y}, \hat{\theta})$ , given the estimates  $\{\hat{\sigma}_{j,m}^2\}_{j,m}$  and  $\hat{\theta}$  from window-level inference. First, we present the Kalman filter/smooth algorithm to compute the mean posterior trajectory, as well as the accompanying credible interval. Next, we present the forward filtering backward sampling (FFBS) algorithm [Carter and Kohn, 1994, Lindsten and Schön, 2013] to generate Monte Carlo (MC) sample trajectories.

First, we define additional notations.

1)  $\tilde{\mathbf{z}}_{j,k|k'} = \mathbb{E}[\tilde{\mathbf{z}}_{j,k} \mid \{\hat{\sigma}_{j,m}^2\}_{j,m}, \mathbf{y}_{1:k'}, \hat{\theta}] \in \mathbb{R}^2$

Posterior mean of  $\tilde{\mathbf{z}}_{j,k|k'}$ . We are primarily concerned with the following three types: 1)  $\tilde{\mathbf{z}}_{j,k|k-1}$ , the one-step prediction estimate, 2)  $\tilde{\mathbf{z}}_{j,k|k}$ , the Kalman filter estimate, and 3)  $\tilde{\mathbf{z}}_{j,k|MN}$ , the Kalman smoother estimate.

2)  $\tilde{\mathbf{z}}_{k|k'} = [(\tilde{\mathbf{z}}_{1,k|k'})^T, \dots, (\tilde{\mathbf{z}}_{J,k|k'})^T]^T \in \mathbb{R}^{2J}$

A collection of  $\{\tilde{\mathbf{z}}_{j,k|k'}\}_j$  in a single vector.

3)  $\mathbf{P}_{j,k|k'} = \mathbb{E}[(\tilde{\mathbf{z}}_{j,k} - \tilde{\mathbf{z}}_{j,k|k'}) (\tilde{\mathbf{z}}_{j,k} - \tilde{\mathbf{z}}_{j,k|k'})^T \mid \{\hat{\sigma}_{j,m}^2\}_{j,m}, \mathbf{y}_{1:k'}, \hat{\theta}] \in \mathbb{R}^{2 \times 2}$

Posterior covariance of  $\tilde{\mathbf{z}}_{j,k|k'}$ . Just as in  $\tilde{\mathbf{z}}_{j,k|k'}$ , we are interested in three types, i.e.,  $\mathbf{P}_{j,k|k-1}$ ,  $\mathbf{P}_{j,k|k}$ , and  $\mathbf{P}_{j,k|MN}$ .

4)  $\mathbf{P}_{k|k'} = \text{blkdiag}(\mathbf{P}_{1,k|k'}, \dots, \mathbf{P}_{J,k|k'}) \in \mathbb{R}^{2J \times 2J}$

A block diagonal matrix of  $J$  posterior covariance matrices.

5)  $\mathbf{A} = \text{blkdiag}(\exp(-\Delta/l_1) \mathbf{R}(\omega_1), \dots, \exp(-\Delta/l_J) \mathbf{R}(\omega_J))$

A block diagonal transition matrix.

6)  $\mathbf{H} = (1, 0, \dots, 1, 0)$  The observation gain.

### Kalman filter/smooth

The Kalman filter equations are given as

$$\begin{aligned}
\tilde{\mathbf{z}}_{j,mN+n|mN+(n-1)} &= \exp(-\Delta/l_j) \mathbf{R}(\omega_j) \tilde{\mathbf{z}}_{j,mN+(n-1)|mN+(n-1)} \\
\mathbf{P}_{j,mN+n|mN+(n-1)} &= \exp(-2\Delta/l_j) \mathbf{R}(\omega_j) \mathbf{P}_{j,mN+(n-1)|mN+(n-1)} \mathbf{R}^T(\omega_j) \\
&\quad + \sigma_{j,m}^2 (1 - \exp(-2\Delta/l_j)) \\
\mathbf{K}_{mN+n} &= \mathbf{P}_{mN+n|mN+(n-1)} \mathbf{H}^T (\mathbf{H} \mathbf{P}_{mN+n|mN+(n-1)} \mathbf{H}^T + \sigma_\nu^2)^{-1} \\
\tilde{\mathbf{z}}_{mN+n|mN+n} &= \tilde{\mathbf{z}}_{mN+n|mN+(n-1)} + \mathbf{K}_{mN+n} (\mathbf{y}_{mN+n} - \mathbf{H} \tilde{\mathbf{z}}_{mN+n|mN+(n-1)}) \\
\mathbf{P}_{mN+n|mN+n} &= (\mathbf{I}_{2J \times 2J} - \mathbf{K}_{mN+n} \mathbf{H}) \mathbf{P}_{mN+n|mN+(n-1)}.
\end{aligned} \tag{34}$$

Subsequently, the Kalman smoother equations are given as

$$\begin{aligned}
\mathbf{C}_{mN+n} &= \mathbf{P}_{mN+n|mN+n} \mathbf{A}^T \mathbf{P}_{mN+(n+1)|mN+n}^{-1} \in \mathbb{R}^{2J \times 2J} \\
\tilde{\mathbf{z}}_{mN+n|MN} &= \tilde{\mathbf{z}}_{mN+n|mN+n} \\
&\quad + \mathbf{C}_{mN+n} (\tilde{\mathbf{z}}_{mN+(n+1)|MN} - \tilde{\mathbf{z}}_{mN+(n+1)|mN+n}) \\
\mathbf{P}_{mN+n|MN} &= \mathbf{P}_{mN+n|mN+n} \\
&\quad + \mathbf{C}_{mN+n} \mathbf{P}_{mN+(n+1)|MN} \mathbf{C}_{mN+n}^T \\
&\quad - \mathbf{C}_{mN+n} \mathbf{P}_{mN+(n+1)|mN+n} \mathbf{C}_{mN+n}^T
\end{aligned} \tag{35}$$

To obtain the mean reconstructed trajectory for the  $j^{\text{th}}$  oscillatory component,  $\{\hat{\mathbf{y}}_{j,k}\}_k$ , we take the real part of the  $j^{\text{th}}$  component of the smoothed mean,  $\hat{\mathbf{y}}_{j,k} = \mathbf{e}_{2j-1}^T \cdot \tilde{\mathbf{z}}_{k|MN}$ , where  $\mathbf{e}_{2j-1} \in \mathbb{R}^{2J}$  is a unit vector with the only non-zero value, equal to 1, at the entry  $2j-1$ .

The 95% credible interval for  $\hat{\mathbf{y}}_{j,k}$ , denoted as  $\text{CI}_{j,k}^{\text{lower}}/\text{CI}_{j,k}^{\text{upper}}$  for the upper/lower end, respectively, is given as

$$\begin{aligned}\text{CI}_{j,k}^{\text{upper}} &= \mathbf{e}_{2j-1}^T \cdot \tilde{\mathbf{z}}_{k|MN} + 1.96 \cdot \sqrt{\mathbf{e}_{2j-1}^T \mathbf{P}_{k|MN} \mathbf{e}_{2j-1}} \\ \text{CI}_{j,k}^{\text{lower}} &= \mathbf{e}_{2j-1}^T \cdot \tilde{\mathbf{z}}_{k|MN} - 1.96 \cdot \sqrt{\mathbf{e}_{2j-1}^T \mathbf{P}_{k|MN} \mathbf{e}_{2j-1}}.\end{aligned}\quad (36)$$

**FFBS algorithm for  $p(\{\mathbf{z}_j\}_j \mid \{\sigma_{j,m}^2\}_{j,m}, \mathbf{y}, \theta)$**

To generate the MC trajectory samples from the posterior distribution  $p(\{\mathbf{z}_j\}_j \mid \{\sigma_{j,m}^2\}_{j,m}, \mathbf{y}, \hat{\theta})$ , we use the FFBS algorithm. The steps are summarized in Algorithm 2, which uses the Kalman estimates derived in the previous section. We denote  $s = 1, \dots, S$  as the MC sample index.

---

**Algorithm 2:** FFBS algorithm

---

**Result:**  $\{\tilde{\mathbf{z}}_k^{(s)}\}_{k,s}^{MN,S}$

**for**  $s \leftarrow 1$  **to**  $S$  **do**

Sample  $\tilde{\mathbf{z}}_{MN}^{(s)}$  from  $\mathcal{N}(\tilde{\mathbf{z}}_{MN|MN}, \mathbf{P}_{MN|MN})$ .

**for**  $k \leftarrow MN-1$  **to**  $1$  **do**

Sample  $\tilde{\mathbf{z}}_k^{(s)}$  from  $\mathcal{N}(\tilde{\mu}_k, \tilde{\mathbf{P}}_k)$ , where

$\tilde{\mu}_k = \tilde{\mathbf{z}}_{k|k} + \mathbf{P}_{k|k} \mathbf{A}^T \mathbf{P}_{k+1|k}^{-1} (\tilde{\mathbf{z}}_{k+1}^{(s)} - \mathbf{A} \tilde{\mathbf{z}}_{k|k})$

$\tilde{\mathbf{P}}_k = \mathbf{P}_{k|k} - \mathbf{P}_{k|k} \mathbf{A}^T \mathbf{P}_{k+1|k}^{-1} \mathbf{A} \mathbf{P}_{k|k}$ .

**end**

**end**

---

## H. Computational efficiency of PLSO vs. GP-PS

We show the runtime of PLSO and piecewise stationary GP (GP-PS) for inference of the mean trajectory of the hippocampus data ( $f_s = 1, 250$  Hz,  $J = 5$ , 2-second window) for varying data lengths (50, 100, 200 seconds corresponding to  $K = 6.25 \times 10^4, 1.25 \times 10^5, 2.5 \times 10^5$  sample points, respectively).

As noted in Section 5, the computational complexity of PLSO is  $O(J^2 K)$ , where as the computational complexity of GP-PS is  $O(N^2 K)$ . Since  $N$ , the number of samples per window, is fixed (2,500 samples), we expect both PLSO and GP-PS to be linear in terms of the number of samples  $K$ . Table 3 indeed confirms that this is the case. However, we observe that PLSO is much more efficient than GP-PS.

Table 3: Runtime (s) for PLSO and GP-PS for varying data length

	PLSO	GP-PS
$T = 50$	1.7	346.8
$T = 100$	3.1	700.6
$T = 200$	6.5	1334.0

## I. Simulation experiment (Section 5.1)

We simulate from the following model for  $1 \leq k \leq K$

$$\mathbf{y}_k = 10 \left( \frac{K-k}{K} \right) \mathbf{z}_{1,k}^{\mathfrak{R}} + 10 \cos^4(2\pi\omega_0 k) \mathbf{z}_{2,k}^{\mathfrak{R}} + \nu_k,$$

where  $\mathbf{z}_{1,k}$  and  $\mathbf{z}_{2,k}$  are from the PLSO stationary generative model, i.e.,  $\sigma_{j,m}^2 = \sigma_j^2$ . The parameters are  $\omega_0/\omega_1/\omega_2 = 0.04/1/10$  Hz,  $f_s = 200$  Hz,  $T = 100$  seconds,  $l_1 = l_2 = 1$ , and  $\nu_k \sim \mathcal{N}(0, 25)$ . This stationary process comprises two amplitude-modulated oscillations, namely one modulated by a slow-frequency ( $\omega_0 = 0.04$  Hz) sinusoid and the other a linearly-increasing signal [Ba et al., 2014]. We assume a 2-second PS interval. For PLSO models, we use  $J = 2$  components and 5 block coordinate descent iterations for optimizing  $\theta$  and  $\{\sigma_{j,m}^2\}_{j,m}$ .

Fig. 6 shows the true data in the time domain and spectrogram results. Fig. 6(c) shows that although the regularized STFT detects activities around 1 and 10 Hz, it fails to delineate the time-varying spectral pattern. Fig. 6(d) shows that PLSO with stationarity ( $\lambda \rightarrow \infty$ ) assumption is too restrictive. Fig. 6(e), (f) show that both PLSO with independent window assumption ( $\lambda = 0$ ) and PLSO with cross-validated  $\lambda$  ( $\lambda = \lambda_{\text{CV}}$ ) are able to capture the dynamic pattern, with the latter being more effective in recovering the smooth dynamics across different PS intervals.

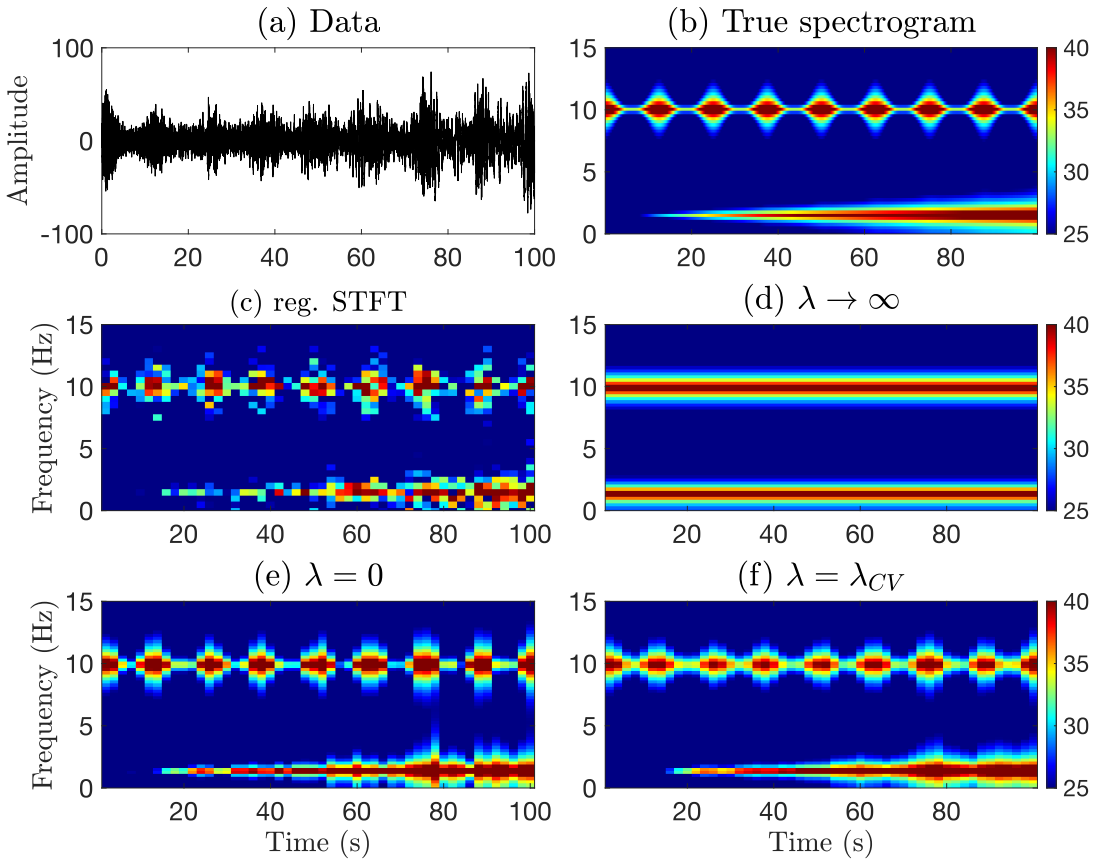


Figure 6: Simulation result with spectrograms (in dB). (a) True data (b) True spectrogram (c) regularized STFT (d) PLSO with  $\lambda \rightarrow \infty$  (e) PLSO with  $\lambda = 0$  (f) PLSO with  $\lambda = \lambda_{CV}$

## J. Details of the TVAR model

As explained in Section 5, the TVAR model is defined as

$$\mathbf{y}_k = \sum_{p=1}^P a_{p,k} \mathbf{y}_{k-p} + \varepsilon_k,$$

which can alternatively be written as

$$\begin{pmatrix} \mathbf{y}_k \\ \vdots \\ \mathbf{y}_{k-P+1} \end{pmatrix} = \underbrace{\begin{pmatrix} a_{1,k} & a_{2,k} & \cdots & a_{P-1,k} & a_{P,k} \\ 1 & 0 & \cdots & 0 & 0 \\ 0 & 1 & \cdots & 0 & 0 \\ \vdots & & \ddots & & \vdots \\ 0 & 0 & \cdots & 1 & 0 \end{pmatrix}}_{A_k} \begin{pmatrix} \mathbf{y}_{k-1} \\ \vdots \\ \mathbf{y}_{k-P} \end{pmatrix} + \varepsilon_k.$$

It is the transition matrix  $A_k$  that determines the oscillatory component profile at time  $k$ , such as the number of components and the center frequencies. Specifically,  $\{A_k\}_k$  are first fit to the data  $\mathbf{y}$  and then eigen-decomposition is performed on each of the estimated  $\{A_k\}_k$ . More in-depth technical details can be found in [West et al., 1999].

We use publicly available code for the TVAR implementation<sup>3</sup>. We use TVAR order of  $p = 70$ , as the models with lower orders than this value did not capture the theta-band signal - The lowest frequency band in these cases were the gamma band ( $> 30$  Hz). Even with the higher orders of  $p$ , and various hyperparameter combinations, we observed that the slow and theta frequency band was still explained by a single oscillatory component. For the discount factor, we used  $\beta = 0.999$  to ensure that the TVAR coefficients and, consequently, the decomposed oscillatory components do not fluctuate much.

## K. Anesthesia EEG dataset (*Section 5.3*)

We show spectral analysis results for the EEG data of a subject anesthetized with propofol (This is a different subject from the main text.) The data last  $T = 2,500$  seconds, sampled at  $f_s = 250$  Hz. We assume a 4-second PS interval, use  $J = 9$  components and 5 block coordinate descent iterations for optimizing  $\theta$  and  $\{\sigma_{j,m}^2\}_{j,m}$ .

Fig. 7 shows the STFT and the PLSO-estimated spectrograms. As noted in the main text, PLSO with stationarity assumption is too restrictive and fails to capture the time-varying spectral pattern. Both PLSO with  $\lambda = 0$  and  $\lambda = \lambda_{CV}$  are more effective in capturing such patterns, with the latter able to remove the artifacts and better recover the smoother dynamics.

<sup>3</sup><https://www2.stat.duke.edu/~mw/mwsoftware/TVAR/index.html>

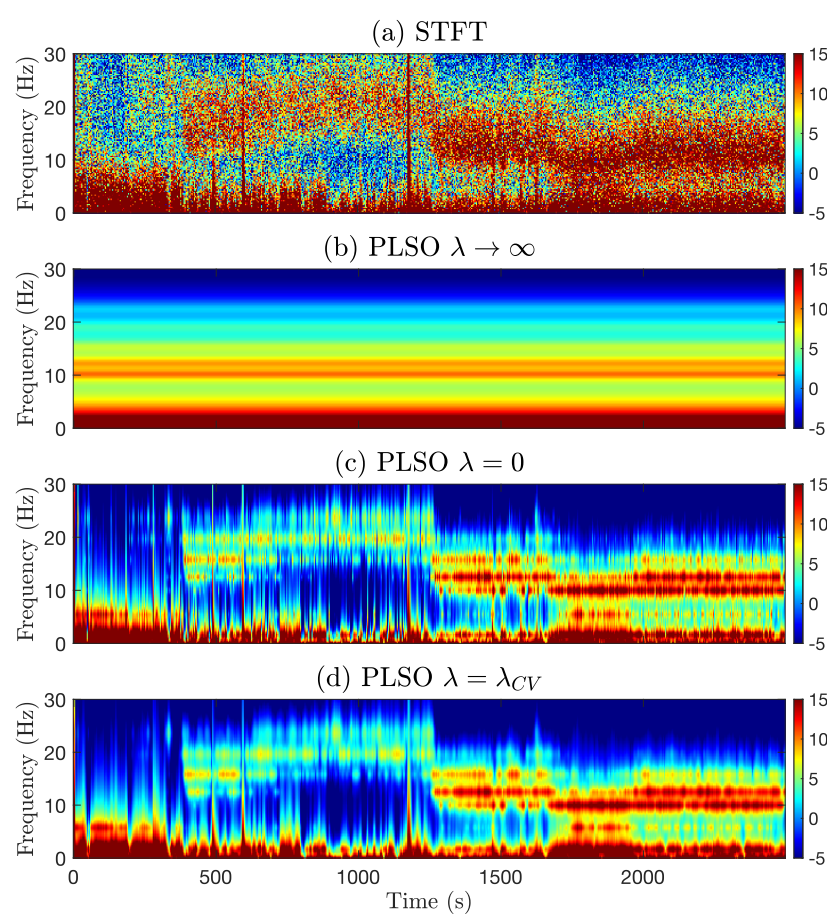


Figure 7: Spectrogram (in dB) under propofol anesthesia. (a) STFT of the data (b) PLSO with  $\lambda \rightarrow \infty$  (c) PLSO with  $\lambda = 0$  (d) PLSO with  $\lambda = \lambda_{CV}$ .